Journal of Cleaner Production 422 (2023) 138636

Contents lists available at ScienceDirect

Journal of Cleaner Production

journal homepage: www.elsevier.com/locate/jclepro

Process development for a novel polygeneration purpose based on tars produced by a biomass gasification unit; feasibility study from the thermodynamic, economic, and environmental viewpoints

Mohamad Abou Houran [a], Mohamed A. Habila [b], Fahid Riaz [c], Manoj Kumar Agrawal [d], Kwanho Shi [e,*]

[a] School of Electrical Engineering, Xi'an Jiaotong University, Xi'an, 710049, China
[b] Department of Chemistry, College of Science, King Saud University, P. O. Box 2455, Riyadh, 11451, Saudi Arabia
[c] College of Engineering, Abu Dhabi University, Abu Dhabi, United Arab Emirates
[d] GLA University, Mathura, UP, 281406, India
[e] Sustainable Management of Natural Resources and Environment Research Group, Faculty of Environment and Labour Safety, Ton Duc Thang University, Ho Chi Minh City, Viet Nam

ARTICLE INFO

Handling Editor: Jin-Kuk Kim

Keywords:
Biomass gasification
Tar
Polygeneration structure
Goswami cycle
CO_2 footprint
Aspen HYSYS

ABSTRACT

The tar produced by biomass gasification can be challenging to handle in processing units. To address this issue, a new polygeneration structure based on tar combustion has been designed in this study. This structure has been developed using Aspen HYSYS software and consists of subsystems, including the tar combustion section integrated with a gas turbine cycle, a low-grade temperature section, a Goswami utility section, and a hydrogen production section. The products of this structure are 7920.65 kg/s of hot water, 33.52 kg/s of cold water, 0.56 kg/s of hydrogen, 4.444 kg/s of oxygen, and 222100 kW of power. The system is examined from various perspectives: energy, exergy, environment, and economics. The overall energy and exergy efficiencies are 89.72% and 54.53%, respectively. The exergy analysis exhibits a total irreversibility of 859,492 kW, in which the low-grade temperature section has the highest exergy destruction with a share of 72%. Accordingly, the environmental analysis demonstrates that the new process has zero indirect carbon dioxide emissions, and its footprint is equivalent to 0.22 kg_{CO2}/kWh. Also, the products have been produced according to economic estimates with a cost of energy of 0.0068 $/kWh and a total unit cost of products of 0.0274 $/GJ.

1. Introduction

The demand for energy sources has been significantly augmented due to industry growth, societal shifting lifestyles, and technological advancements (Guedri et al., 2023; Jiang et al., 2023; Rokhmawati et al., 2023; Suleman et al., 2014). Using fossil fuels and hydrocarbons as energy sources has been instrumental in satisfying fundamental energy requirements in recent decades. However, these resources' adverse environmental impact and limited availability have presented considerable limitations (Y. Chen et al., 2021; H.-M. Li et al., 2023; Rahimpour et al., 2012; Ramesh et al., 2023). Considering the advancements in energy conversion knowledge, exploiting renewable energy sources such as geothermal, wind, solar, and biomass feedstock has been implemented as an effective strategy to address previous limitations (Guo et al., 2020; X. Liu et al., 2023a; Lv et al., 2023; MosayebNezhad et al., 2019). Biomass fuel sources can exhibit significant energy density owing to their gasification and combustion processes. Hence, it exhibits the most pronounced congruence with traditional energy sources among the options of sustainable energy (P. Ahmadi et al., 2013; Razeghi et al., 2014; Sun et al., 2023). The gasification procedure encompasses a sequence of sequential stages, beginning with the reactor drying phase, followed by pyrolysis, and concluding with the gasification step. Numerous subsequent chain reactions occur during the gasification stage (Haghghi et al., 2019; Yu et al., 2023). The gaseous stream generated as a result predominantly consists of methane, hydrogen, carbon dioxide, carbon monoxide, and nitrogen. The gaseous stream exhibits particulates, ammonia, nominal sulfur compounds, and tar, which are considered atmospheric waste topping (B. Wang et al., 2023b). Synthesis gas production occurs when the gaseous output

* Corresponding author.
E-mail address: kwanhoshi58@gmail.com (K. Shi).

https://doi.org/10.1016/j.jclepro.2023.138636
Received 18 June 2023; Received in revised form 28 August 2023; Accepted 30 August 2023
Available online 1 September 2023

Nomenclature

A	Area
$\dot{C}$	Cost rate
e	Specific exergy
e_l^{ch}	Standard molar chemical exergy
$\dot{E}_D$	Exergy destruction
$\dot{E}$	Exergy rate
F	Molar flow rate
h	Specific enthalpy
l	Annual interest rate
LHV	Lower heating value
$\dot{m}$	Mass flow rate
P	Pressure
P_c	Critical pressure
$\dot{Q}$	Thermal energy rate
R	Universal gas constant
s	Specific entropy; Lifetime of the cycle
T	Temperature
T_c	Critical temperature
U	Overall heat loss coefficient
$\dot{W}$	Power
x	Molar fraction
Z	Purchase cost

Greek symbols

η	Isentropic efficiency
$\in_{CO_2}$	Specific CO_2 emission
ω	Energy efficiency
Ψ	Exergy efficiency

Subscripts and Superscripts

0	Reference state
C	Cold
ch	Chemical
dest	Destructions
el	Electricity
en	Energy
ex	Exergy
F	Fuel
H	Hot
in	Input
out	Output
P	Product
ph	Physical

Abbreviations

CCHP	Combined cooling, heat, and power
CHP	Combined heat and power
COE	Cost of energy
CRV	Catalytic reactor volume
E-i	i-th heat exchanger
GTC	Gas turbine cycle
GUS	Goswami utility section
ICF	Income cash flow
HPS	Hydrogen production section
K-i	i-th compressor
LGTS	Low-grade temperature section
MSW	Municipal solid waste
NPV	Net present value
ORC	Organic Rankine cycle
P-i	i-th pump
S-i	i-th separator
SCE	Specified CO_2 emissions
SOFC	Solid oxide fuel cell
SRC	Steam Rankine cycle
TAC	Total annual cost
TCS	Tar combustion section
TUCP	Total unit cost of product
T-i	i-th turbine
VLV-i	i-th valve
X-i	i-th membrane

undergoes a series of cleaning, reforming, and displacement processes. The present discourse offers a comprehensive literature review that critically examines studies focusing on the employment of biomass fuel within energy conversion systems.

Wei et al. (X. Wei et al., 2020) compared the viability of using coal and biomass fuels for oxy-fuel combustion combined with a supercritical CO_2 cycle. They found that the coal-based scheme had an exergy efficiency of 30.5%, while the biomass-fueled showed 28.1%. They stated that the biomass-driven system became economically feasible when the carbon tax exceeded 24 €/ton_{CO2}. Zhang et al. (Zang et al., 2020) executed a comparative investigation of eight biomass-integrated gasification combined cycles for electric power production. They found that these approaches have a low global warming potential of less than 240 kg_{CO2}/MWh and have the prospect of diminishing emissions from the electricity grid. Hidrovo et al. (Briones-Hidrovo et al., 2021) analyzed the thermodynamic and environmental aspects of generating electricity from residual forest biomass. They compared the gasification and combustion methods and found that the former had superior environmental performance. Moreover, they demonstrated that the gasification process could achieve an energy efficiency of up to 57%. Roy et al. (2019) examined the economic and environmental benefits of a biomass-based integrated power plant that utilized externally fired gas turbine cycle (GTC), a solid oxide fuel cell (SOFC), and an organic Rankine cycle (ORC). The system achieved a high level of efficiency at 49.5% and also had a low cost of electricity at 0.086 $/kWh. Furthermore, the plant could reduce the maximum amount of CO_2 emissions by up to 3564 ton_{CO2}/year. Anvari et al. (2019) proposed a new way to generate 15 MW of power using a hybrid biomass-solar combined cycle. The system included a GTC that utilized biomass raw material, a heliostat solar field to assist the GTC in the second loop, and a steam Rankine cycle (SRC). The system achieved an exergy efficiency of 33.4%, resulting in a 49% reduction in CO_2 emissions compared to a standalone biomass-fueled power plant. Cardoso et al. (2019) conducted a study on the possibility of using forest biomass blends gasification to feed an 11 MW power plant in Portugal. The study revealed that the net present value and payback period were 2.37 M€ and 23.1 years, respectively.

In addition to biomass-based combined power plants, some studies have explored implementing alternative energy cycles for cogeneration or multigeneration purposes. Hence, a combination of biomass power plant and compressed air energy storage was used for a combined heat and power (CHP) application by Razmi et al. (2021). They found that municipal solid waste (MSW) was the most promising biomass feedstock, offering the highest total efficiency compared to other feedstocks. According to a study conducted by Cao et al. (Cao et al., 2021), a plant that utilized a biomass gasifier, a supercritical CO_2 cycle, and a domestic water heater to support a CHP application was developed. They employed a bat optimization method to identify the most effective operating points, resulting in an optimal exergy efficiency of 38.4%. The optimum unit cost of products and the optimum levelized CO_2 emissions were determined to be 7.5 $/GJ and 0.476 ton/MWh, correspondingly. Ji-chao and Sobhani (Ji-chao & Sobhani, 2021) incorporated a biomass gasification unit with a GTC and designed supercritical CO_2 and Kalina cycles as the bottoming unit for a CHP application. The exergy efficiency and the payback period were found at 40.97% and 6.9 years, correspondingly. In a study by Hamedani et al. (2023), different small-scale biomass-fed combined cooling, heating, and power (CCHP) arrangements were compared in terms of a thermo-environmental study. The researchers found that incorporating gasification with an internal combustion engine and a heat pump was the most sustainable option based on different indicators. Udeh et al. (2021) thoroughly evaluated a micro-CCHP system driven by biomass fuel, encompassing an ORC, a Stirling engine, a chiller, and a heating provider unit. They analyzed the effects of various important factors and fuel quality on the CCHP system. They noted that the designed CCHP system resulted in significant primary energy savings and reduced CO_2 emissions by 55% and 43% when using woodchips as fuel, respectively. Jia et al. (2021) studied a CCHP system that included biomass gasification, a SOFC, a micro-gas turbine, an absorption chiller, and a heating provider unit. They encountered that the system had an exergy efficiency of over 40% and a payback period of approximately 7–8 years. Xie et al. (2023) proposed an integrated CCHP system that used biomass gasification, a low-temperature fuel cell, an absorption chiller, and a heating provider unit. The system's energy and exergy efficiencies were calculated at 57.4% and 18.1%, correspondingly. The design of a CCHP system powered by a combination of municipal solid waste and natural gas was performed by Asgari et al. (2020). The system included a gasification unit, a gas turbine cycle, a heating provider unit, and an absorption chiller. The results showed an annual energy utilization factor of 71.2% and an exergy efficiency of 30.8% when producing 27.4 kW of electric power.

Certain studies have explored the integration of hydrogen production subsystems with biomass-driven cogeneration or multigeneration systems. In a study by Fan et al. (G. Fan et al., 2021), a multigeneration system was examined, including a GTC, an absorption chiller, and a Copper–Chlorine thermochemical process. This system was capable of producing electricity, coolant, and hydrogen simultaneously. The study found that the system had an exergy efficiency of 44% and a payback period of 2.5 years. Wang et al. (D. Wang et al., 2023) studied a system that generated electricity and hydrogen using biomass fuel and geothermal energy. The system incorporated a GTC, a geothermal-assisted SRC, and a water electrolyzer. With optimal conditions, the cogeneration framework achieved an energy efficiency of 42.4% and a unit cost of products at 68.5 $/MWh. Ghorbannejad et al. (2022) suggested a system that combined steam biomass gasification and SOFC to generate hydrogen, CO_2, and electricity for multiple purposes. The study analyzed the exergoeconomic and exergoenvironmental factors. Lin et al. (2022) developed an efficient biomass gasification hybrid system to generate power and liquid hydrogen. The system consisted of a GTC, an SRC, a water electrolyzer unit, and a hydrogen liquefaction cycle. The system was capable of producing up to 3377 kW of power and 14.8 kg/h of hydrogen. The total cost rate was minimized to 86.61 $/h, while the environmental impact was kept low with an optimal index of 1.09 kg_{CO_2}/kWh. A study by Wang et al. (J. Wang et al., 2022) evaluated a multigeneration system that utilized biomass fuel to produce electricity, hydrogen, and freshwater. The system used a solid oxide electrolyzer, a multi-effect desalination, and a SRC. The products generated had an energy efficiency of 36.4% and a unit cost of 16.6 $/GJ.

Various types of gasification reactors are utilized for biomass gasification, such as updraft fixed bed, down draft fixed bed, and bubbling fluidized bed configurations. The downdraft fixed bed reactor is found to generate a relatively small amount of tar, whereas the updraft fixed bed reactor has been observed to produce the highest quantity of tar (Ersöz et al., 2018). Tar is a complex amalgamation of organic compounds generated as a result of the thermal conversion process of biomass. It occurs due to incomplete combustion or pyrolysis mechanisms comprising heavy, sticky, and toxic substances. Tar can adversely impact the conversion equipment's performance, resulting in fouling, corrosion, and operational challenges. Hence, the removal or decomposition of tar is imperative prior to the efficient utilization of biomass (J. Li et al., 2021).

Several techniques are utilized for the tar treatment in biomass processing. The most significant techniques are provided in the following:

- Tar filtration: This technique involves the utilization of ceramic, metallic, or fabric filters in order to effectively capture and eliminate tar particles present within the biomass gas or syngas stream (Bhaduri et al., 2015).
- Tar cracking: This method refers to exposing biomass gas or syngas to elevated temperatures, typically ranging from 500 to 1000 °C, under the influence of a catalyst. The catalyst facilitates the decomposition of intricate tar compounds into more straightforward, less deleterious gases such as methane, carbon monoxide, and hydrogen. This procedure is conducted within specialized tar cracking reactors (J. S. Wang et al., 2022).
- Tar reforming: This method is the process of converting tar into beneficial syngas through the reaction of tar with steam or air at high temperatures. This chemical reaction facilitates the conversion of the constituents of tar into carbon monoxide and hydrogen, two valuable substances that can be subsequently employed for the purpose of energy production (Ren et al., 2021).
- Catalytic tar reduction: This method involves the utilization of a catalyst to undergo chemical reactions with tar constituents, converting them into more elemental and environmentally benign gases. The catalyst facilitates the process of tar decomposition or reforming, leading to the formation of simpler chemical compounds (Anis and Zainal, 2011).

The utilization of tar obtained through biomass gasification commonly needs to be improved in biomass processing systems. Numerous energy conversion systems utilizing synthesis gases derived from biomass processing have been devised; however, more attention must be directed toward using tar as a viable fuel source. To address this gap, the current study examines the viability of employing an auxiliary multigeneration system in combination with a biomass raw material processing unit. In this context, the primary innovations and novelties associated with the present study are as follows:

- The utilization of tar derived from biomass processing was previously not incorporated in the biomass-based energy applications. Hence, the present study explores the feasibility of employing tar as a primary fuel source for a novel energy system through the development and application of an appropriate conversion method.
- The present design has effectively reduced the CO_2 footprint by generating multiple outputs such as electricity, hot water, chilled water, oxygen, and hydrogen through the utilization of a novel thermal integration application.

Therefore, tar is used as an energy source for a GTC, an ORC-based low-grade temperature unit, a Goswami utility unit, and a water electrolysis unit for hydrogen production. The system configuration is simulated within the Aspen HYSYS software, wherein a thorough investigation encompassing energy, exergy, economic, and environmental considerations is undertaken. Furthermore, a sensitivity analysis is conducted to investigate the influence of operational parameters on the critical variables.

2. Process description

In this study, a new process has been introduced that, in addition to high energy and exergy efficiency, is capable of producing its energy and exergy products with a low CO_2 footprint. For this purpose, the energy source of this new process is tars derived from biomass gasification, which is usually a challenge in the biomass processing system. Here, they are used as an energy source for producing utility heat, cooling, electricity, hydrogen, and oxygen (the products are shown in Fig. 1).

The new process in terms of energy source and integration connection between subsystems is entirely new. An extensive heat exchanger network has been defined for recovering waste heat in this new process. Moreover, efforts have been made to maximize heat recovery in the direction of energy integration to increase energy and exergy efficiency and reduce pollution intensity. The proposed system consists of the following subsystems:

- Tar combustion section (TCS): In this section, the products of biomass gasification, known as Tars, are burned with the oxygen present in the air. They are also used at high temperatures to produce domestic hot water and supply heat to the organic Rankine cycle. This section releases the flue gas into the atmosphere after producing DHW products.
- Low-grade temperature section (LGTS): In the proposed structure, a large portion of the heat from hot flue gases (resulting from the combustion of tars) is provided to the organic Rankine cycle with octane working fluid. It is worth noting that this working fluid has been selected because simple cooling is not used in the octane condensation section. Instead, the high temperature of the octane fluid output from the expansion turbine is used in three parallel stages. This hot stream is used as a heat source for three separate cycles. A portion of this hot fluid is used in the Goswami subsystem. The other portion of the hot octane fluid is split into two parts. Each part is used in organic Rankine cycles with heptane and pentane as working fluids. Again, the high-temperature fluids exiting from the turbines produce domestic hot water in the two mentioned ORCs for greater heat integration. As a result, the consumption of utility cooling water for condensing working fluids in organic Rankine cycles has been eliminated, leading to significant savings. Therefore, the LGTS subsystem consists of three integrated organic Rankine cycles, which work with octane, heptane, and pentane as working fluids.
- Goswami utility section (GUS): The primary purpose of this subsystem is to produce power, cooling or cold water, and heating or DHW (at a temperature of 50 °C). In this cycle, a portion of the octane hot fluid heats the reboiler of the regeneration column. As a result, ammonia is enriched in the vapor phase and produces power through expansion in the turbine. The low temperature of the fluid exiting the turbine produces cold water with a temperature of 15 °C in an evaporator. After heat transfer in the reboiler and superheater, the remaining heat of the octane hot fluid is used for DHW production.
- Hydrogen production section (HPS): A portion of the power generated in the LGTS subsystem is used to supply power to the HPS subsystem. For this purpose, hydrogen and oxygen are produced through water electrolysis using the PEM method. This method of hydrogen production has the lowest pollution compared to thermochemical systems. As shown in Fig. 1, hydrogen produced from this new process can be used as fuel, and oxygen also has urban and hospital uses.

In addition, the primary advantages of the proposed system can be succinctly outlined as follows:

- The utilization of biomass tar feed, which needs more functional and practical examinations.
- Implementing comprehensive thermal integration throughout all components of the novel process is considered a crucial consideration.
- The production of hydrogen through efficient and environmentally-friendly processes with minimal pollutant emissions has been employed.
- Greater efficiencies in terms of energy and exergy have been attained in comparison to previous studies.
- The CO_2 footprint associated with the proposed structure exhibits a low environmental impact compared to previous studies within the same field.

Also, the primary limitations within the proposed system's scope can be categorized as follows:

- The suggested system has employed the by-product generated through biomass upgrading, necessitating a biomass upgrading unit or purchasing raw materials from the biomass upgrading process.
- The limited availability of the corresponding fuel resources constrains the selection of the proposed system's location.
- The utilization of intermediate heat exchangers can give rise to operational constraints due to the thermal integration structure employed.
- The proposed system's successful protection and maintenance necessitates employing skilled workforces.

2.1. *Tar combustion section*

The primary input of this process comprises tars, which are derived through the process of biomass gasification. The compositions and

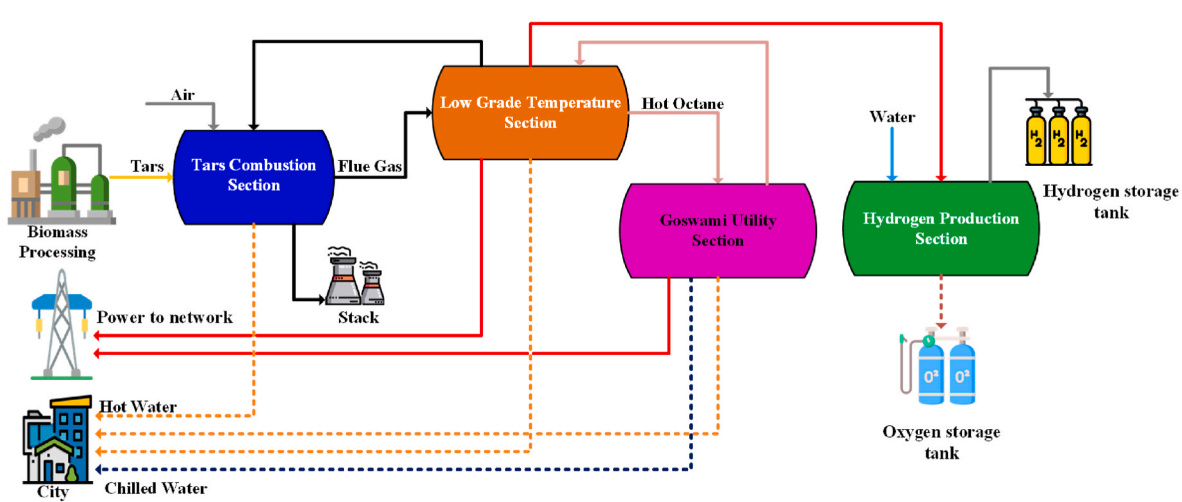

Fig. 1. Overall flow diagram of the integrated polygeneration process.

ultimate analysis of the materials are displayed in Table 1.

According to Fig. 2, air, as an oxidizing agent (stream 2), is reached the same pressure as the feed stream (stream 1) through the compressor K-100. The air and fuel are mixed in the mixer (stream 3) and enter the combustion chamber (CRV-100). Where methane, hydrogen, carbon monoxide, and benzene react with oxygen (Eq. (1) to Eq. (4)). These reactions are exothermic and produce a significant amount of energy.

$$CH_4 + 2O_2 \rightarrow Heat + CO_2 + 2H_2O \quad (1)$$

$$H_2 + 0.5O_2 \rightarrow Heat + H_2O \quad (2)$$

$$CO + 0.5O_2 \rightarrow Heat + CO_2 \quad (3)$$

$$C_6H_6 + 7.5O_2 \rightarrow Heat + 6\ CO_2 + 3H_2O \quad (4)$$

The hot gases exiting the combustion chamber (stream 5) enter the E−101 heat recovery exchanger after passing through heat exchanger E−100 (stream 7). At this point, DHW product (stream 63) is produced from the high temperature of the flue gases. This heat exchanger's flue gases (stream 61) are released through the stack.

2.2. Low-grade temperature section

In Fig. 2, the process flow diagram for this section is shown. The LGTS subsystem consists of three ORCs.

- Organic Rankine cycle with octane as the working fluid: To have an efficient organic Rankine cycle, its working fluid should have a high critical temperature so that the recovered waste heat can be used for higher efficiency. Regular octane is a joint working fluid in organic Rankine cycles with a relatively high critical temperature (569 K). This working fluid, similar to the work done by Ahmadi et al. (P. Ahmadi et al., 2013), has also been used in this article. Octane fluid (stream 8) is evaporated in the E−100 evaporator and is expanded through the T-100 turbine (stream 10). Power is generated through this process, and some of this power is consumed internally (supporting PEM electrolyzers, pumps, and compressors). The hot fluid exiting the turbine is divided into two streams (streams 11 and 12). Stream 11 is sent to the GUS subsystem, and stream 12 is divided into streams 41 and 42 and feeds two other ORC cycles. After streams 38, 43, and 51 have performed heat transfer in their respective subsystems, they are remixed (stream 59). Then, through the P-103 pump, higher-pressure octane fluid feeds the E−100 evaporator.
- Organic Rankine cycle with heptane working fluid: The hot octane stream (stream 41) drives the organic Rankine cycle with heptane working fluid. This working fluid has been previously used by Liao et al. (2020). E−108 evaporator evaporates the heptane stream and feeds the T-012 turbine through it. Due to its desired temperature, the output from this turbine (stream 46) is used to produce DHW product at a temperature of 50 °C in the E−109 heat exchanger. Finally, the working fluid (stream 47), which has wholly liquefied, is sent back to the E−108 heat exchanger through the P-101 pump (Fig. 2).
- Organic Rankine cycle with pentane working fluid: Similar to the organic Rankine cycle with heptane working fluid, this cycle also recovers waste heat from the hot octane stream. E−100 Evaporator is fed with stream 42 (heat source) to evaporate the pentane working fluid. This working fluid has been previously used by Liao et al. (2020). Stream 52 is sent to the evaporator through the P-102 pump. Then it enters the T-103 turbine in vapor form with higher energy content (stream 53), generating power from pentane expansion. Like the previous cycle, the DHW product with a temperature of 50 °C is produced through the E−111 heat exchanger for further heat recovery (stream 57). Therefore, the working fluid is completely condensed without using cooling water utility and is again directed towards the cycle's evaporator through the P-102 pump (Fig. 2).

Table 1
Composition and ultimate analysis of tar stream exiting from biomass gasification (Ersöz et al., 2018).

Components	Mole %
H_2O	8.21
H_2	18.32
Methane	4.2
Nitrogen	39.54
benzene	0.2
CO	14.21
CO_2	15.32

2.3. Goswami utility section

As shown in Fig. 2, stream 11, the hot octane working fluid, is the driving force of the GUS cycle. This cycle uses the NH_3–H_2O mixed working fluid (Vidal et al., 2006), producing cold water, power, and DHW. However, this subsystem (Vidal et al., 2006) does not produce conventional DHW in the conventional form. This product in the structure presented in this article has been added to the Goswami conventional cycle to provide better results. The ammonia-water mixture (stream 14) reaches a higher pressure with a pump P-100. After branching into streams 15 and 16, it feeds two heat exchangers, E−103 and E−101. In heat exchanger E−101, the working fluid is preheated (stream 18) and enters the C-100 column, where working fluid evaporation occurs. Then, concentrated ammonia vapor (stream 19) is produced from the top of the column. The reboiler output of the mentioned column (stream 20) is also used to increase the temperature of the working fluid. The octane working fluid heats the reboiler and the superheat exchanger (E−104). Ammonia vapor enters the T-101 turbine in the form of superheat (stream 28) through the E−104 heat exchanger and expands, generating power which is one of the products of the system. The ammonia stream exiting the turbine (stream 30) acts like a refrigerant with low temperature due to pressure drop. It is used to produce cold water in the E−105 heat exchanger. Stream 34, a mixture of water-ammonia, is passed through the VLV-100 throttling valve, and its pressure is equal to the outlet stream pressure of the turbine T-101. Stream 36, the mixture of streams 33 and 35, is wholly liquefied through the heat exchanger E−106 and returned to the pump P-100.

2.4. Hydrogen production section

To produce renewable hydrogen, this subsystem uses PEM electrolyzer technology (Baak et al., 2019; X. Liu et al., 2023b). In this subsystem, water is used as the fuel for the electrolyzer (stream 66), which enters the electrolyzer stack (CRV-101) at a pressure of 5000 kPa (stream 5) (X. Liu et al., 2023b). The overall reaction of converting water to hydrogen and oxygen occurs using the power supplied by the T-100 turbine. Then, through two membranes X-100 and X-101, hydrogen (stream 71) and oxygen (stream 73) are obtained, respectively. As shown in Fig. 2, hydrogen is used for fuel, and oxygen is suitable for urban and household uses.

3. Material and methods

3.1. Process simulation

Fig. 3 shows the schematic simulation of the proposed process using Aspen HYSYS. The most critical applications of Aspen HYSYS are performance evaluation, process troubleshooting, problem-solving, making changes to operational conditions, and predicting results. This software can easily simulate and optimize even complex units such as refineries for design, development, operation improvement, and problem-solving quickly. This simulation is completed in several stages: important

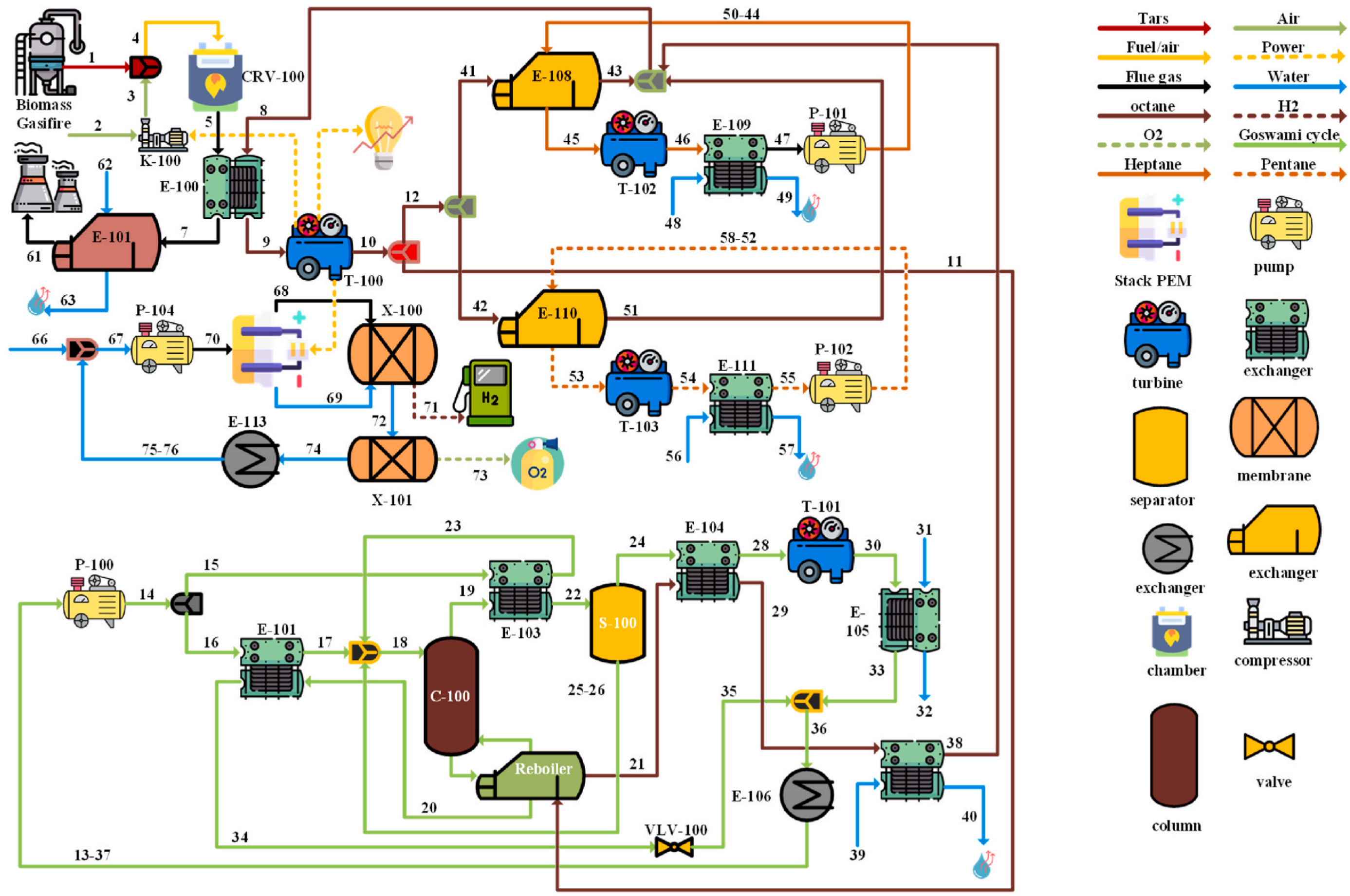

Fig. 2. Process flow diagram for proposed process.

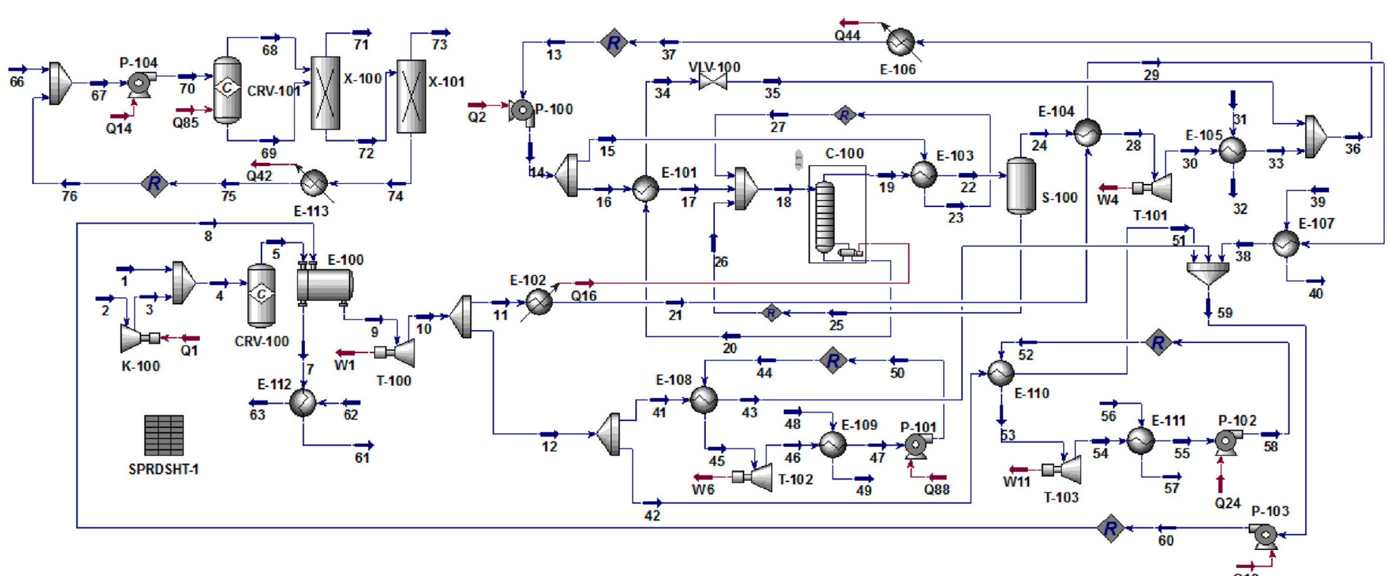

Fig. 3. Schematic simulation of the proposed process in Aspen HYSYS software environment.

input information for defining streams and specifying equipment (Table 2), selecting simulation materials (H2O, O_2, H_2, CH_4, N_2, C_6H_6, octane, CO, CO_2, NH_3, heptane, pentane), selecting a fluid package for estimating thermodynamic properties, defining reactions, and selecting equipment in the Aspen HYSYS flow sheet.

In this article, Peng Robinson's equation of state has been used to simulate the entire process. The Peng Robinson package solves the three-phase, two-phase, and single-phase systems with high efficiency and reliability. It is applicable in a wide range of operating conditions (Xiao et al., 2023). This equation of state, represented by the general form of Eq. (5), was previously utilized by R. Mansouri et al. to model an absorption-chiller cycle using ammonia-water as a working fluid

Table 2
Important information for Aspen HYSYS simulation.

Tars Combustion Section	
Combustor Pressure (kPa)	200
Air to fuel ratio (mass basis)	1.65
Tars Temperature (°C) (Ersöz et al., 2018)	700
Tars Pressure (kPa) (Ersöz et al., 2018)	200
Air inlet temperature (°C)	25
Air inlet Pressure (kPa)	101.3
Domestic hot water temperature (°C) (P. Ahmadi et al., 2011)	50
Flue gas outlet temperature from process (°C)	70.11 (sat vapor)
Low-Grade Temperature Section (P. Ahmadi et al., 2013; Liao et al., 2020)	
Octane-ORC (P. Ahmadi et al., 2013)	
T-100 inlet pressure (kPa)	2000
T-100 outlet pressure (kPa)	28.09
P-103 inlet pressure (kPa)	28.09
P-103 outlet pressure (kPa)	2000
T-100 inlet temperature (°C)	400
heptane-ORC (Liao et al., 2020)	
T-102 inlet pressure (kPa)	1000
T-102 outlet pressure (kPa)	7.847
P-101 inlet pressure (kPa)	7.847
P-101 outlet pressure (kPa)	1000
Working fluid condition from evaporator	Saturated vapor
E−108 pressure drop	0.0
Working fluid condition from condenser	Saturated liquid
Pentane-ORC (Liao et al., 2020)	
T-103 inlet pressure (kPa)	736.9
T-103 outlet pressure (kPa)	109.9
P-102 inlet pressure (kPa)	109.9
P-102 outlet pressure (kPa)	736.9
Working fluid condition from evaporator	Saturated vapor
E−108 pressure drop	0.0
Condensation temperature (°C)	30.19
Hydrogen Production Section (X. Liu et al., 2023b)	
PEM stack pressure (kPa)	5000
PEM stack temperature (°C)	79.9
P-104 outlet pressure (kPa)	5000
Hydrogen pressure (kPa)	4900
oxygen pressure (kPa)	4850
E−113 pressure drop (kPa)	47
E−113 outlet temperature (°C)	70.1
Goswami Utility Section (Vidal et al., 2006)	
Working fluid	Ammonia-water
P-100 outlet pressure (kPa)	2050
P-100 inlet pressure (kPa)	150
C-100 reboiler temperature (°C)	125
T-101 outlet pressure (kPa)	2050
T-101 inlet pressure (kPa)	150
C-100 pressure drop (kPa)	0.0

(Mansouri et al., 2015).

$$P = \frac{RT}{V-b} - \frac{a}{(V^2+bV)+(bV-V^2)} \tag{5}$$

In Eq. (5), P represents pressure, R is the gas constant, T is temperature, and V is the molar volume of the mixture. In addition, a and b are constants of the equation of state, which are defined according to Eq. (6) and Eq. (7) (Lopez-Echeverry et al., 2017; Mansouri et al., 2015; Yang et al., 2019).

$$b = \sum x_i \left(0.07780 \frac{RT_{ci}}{P_{ci}}\right) \tag{6}$$

$$a = \sum_i \sum_j x_i x_j \left[a_i a_j\right]^{0.5} \times \left(1 - k_{ji}\right) \tag{7}$$

In Eq. (6) and Eq. (7), x represents mole fraction, T_c is critical temperature, and P_c is critical pressure. The Peng Robinson equation of state has previously been used by Xiao et al. (X. Liu et al., 2023b) in Aspen HYSYS modeling. This article uses a conversion reactor model to simulate the combustor. It is assumed that all combustible materials are completely burned with air oxygen, and the reaction products are only CO_2 and water vapor (Eq. (1) to Eq. (4)). The use of this reactor model for the combustor has previously been accepted by Rahimpour et al. (2012). The PEM electrolyzer in this article is modeled as a conversion reactor. Moreover, only the overall reaction (Eq. (8)) is defined (Chitsaz et al., 2019; Yu et al., 2023), and its conversion rate is mentioned in Table 1. Other researchers have also accepted this method of defining the PEM electrolyzer in Aspen HYSYS (Azariyan et al., 2021; X. Liu et al., 2023b).

$$H_2O \underset{\dot{W}}{\rightarrow} H_2 + \frac{1}{2}O_2 \tag{8}$$

3.2. Validation of the system

The outcomes obtained through the implementation of the Aspen HYSYS software associated with the proposed system are subjected to comparison with prior studies, as presented in Tables 3 and 4.

Table 3 presents the outcomes derived from the numerical simulation of the ORC, compared with the study conducted by Ahmadi et al. (P. Ahmadi et al., 2013). The present table comprehensively evaluates the operating conditions of key variables, specifically pressure and temperature. It is evident that the achieved outcomes are in substantial concurrence with the referenced article.

Table 4 presents the outcomes derived from the simulation of the PEM electrolyzer compared with the findings obtained by Liu et al. (X. Liu et al., 2023b). In the presented table, an evaluation of several operational variables is conducted. Given the proximity of the results, the simulated model demonstrates a high level of justification and accuracy.

This section suggests significant concordance between the Aspen HYSYS software and the outcomes obtained from reference articles. This observation implies that the Peng Robinson fluid package has been suitably employed for the purposes of simulation. Additionally, it can be utilized with considerable precision for simulating analogous systems.

4. Analysis of the process

4.1. Energy analysis

The primary energy conservation equation is used for a control volume system to evaluate the first law of thermodynamics. In this equation, $\dot{Q}$, $\dot{W}$, h, and $\dot{m}$ represent heat rate, power, specific enthalpy, and mass flow rate, respectively. Additionally, based on Eq. (9), basic equations for energy conservation around the equipment used in the proposed system are listed in Table 5 (H. Chen et al., 2023; Tabriz et al., 2022).

Table 3
Comparing the simulation results obtained for the ORC using octane as working fluid and Ref. (P. Ahmadi et al., 2013).

Parameters	Ref (P. Ahmadi et al., 2013)	This Study	Relative error (%)
Turbine inlet/outlet pressure (kPa)	2000/28.09	2000/28.09	0/0
Turbine inlet/outlet temperature (°C)	400/335.7	400/329.1	0/1.96
Pump inlet/outlet pressure (kPa)	28.09/2000	28.09/2000	0/0
Pump inlet/outlet temperature (°C)	85/85	84.96/85.9	0.04/1.05
Condenser inlet/outlet temperature (°C)	85/400	85.9/400	1.05/0

Table 4
Comparing the simulation results obtained for the PEM electrolyzer and Ref. (X. Liu et al., 2023b).

Parameters	Ref (X. Liu et al., 2023b)	This Study	Relative error (%)
Stack pressure (kPa)	5000	5000	0
Stack temperature (°C)	79.9	79.9	0
Hydrogen temperature (°C)	80	80	0
Hydrogen pressure (kPa)	4900	4900	0
Oxygen temperature (°C)	80.1	80.1	0
Cooler inlet/outlet temperature (°C)	80.1/70.1	80.1/ 70.1	0
Cooler inlet/outlet pressure (kPa)	4706/4659	4706/ 4659	0
Hydrogen mole fraction in top stack	0.6595	0.66	0.07
Oxygen mole fraction in top stack	0.3297	0.33	0.09
Water mole fraction in top stack	0.0108	0.0115	6.08
Stack conversion (%)	75.4	75.4	0

Table 5
Energy conservation equations for the used equipment.

Components	Equations
K-100	$\dot{m}_2h_2 + \dot{W} = \dot{m}_3h_3$
CRV-100	$\dot{m}_4h_4 = \dot{m}_5h_5$
E−100	$\dot{m}_5h_5 + \dot{m}_8h_8 = \dot{m}_9h_9 + \dot{m}_7h_7$
T-100	$\dot{m}_9h_9 = \dot{m}_{10}h_{10} + \dot{W}$
E−112	$\dot{m}_7h_7 + \dot{m}_{62}h_{62} = \dot{m}_{63}h_{63} + \dot{m}_{61}h_{61}$
P-104	$\dot{m}_{67}h_{67} + \dot{W} = \dot{m}_{70}h_{70}$
CRV-101	$\dot{m}_{70}h_{70} + \dot{W} = \dot{m}_{68}h_{68} + \dot{m}_{69}h_{69}$
X-100	$\dot{m}_{68}h_{68} + \dot{m}_{69}h_{69} = \dot{m}_{71}h_{71} + \dot{m}_{72}h_{72}$
X-101	$\dot{m}_{72}h_{72} = \dot{m}_{73}h_{73} + \dot{m}_{74}h_{74}$
E−113	$\dot{m}_{74}h_{74} = \dot{Q} + \dot{m}_{75}h_{75}$
E−108	$\dot{m}_{41}h_{41} + \dot{m}_{44}h_{44} = \dot{m}_{43}h_{43} + \dot{m}_{45}h_{45}$
T-102	$\dot{m}_{45}h_{45} = \dot{W} + \dot{m}_{46}h_{46}$
E−109	$\dot{m}_{48}h_{48} + \dot{m}_{46}h_{46} = \dot{m}_{49}h_{49} + \dot{m}_{47}h_{47}$
P-101	$\dot{m}_{47}h_{47} + \dot{W} = \dot{m}_{50}h_{50}$
E−110	$\dot{m}_{42}h_{42} + \dot{m}_{52}h_{52} = \dot{m}_{51}h_{51} + \dot{m}_{53}h_{53}$
T-103	$\dot{m}_{53}h_{53} = \dot{W} + \dot{m}_{54}h_{54}$
E−111	$\dot{m}_{56}h_{56} + \dot{m}_{54}h_{54} = \dot{m}_{55}h_{55} + \dot{m}_{57}h_{57}$
P-102	$\dot{m}_{55}h_{55} = \dot{W} + \dot{m}_{58}h_{58}$
P-103	$\dot{m}_{59}h_{59} + \dot{W} = \dot{m}_{60}h_{60}$
P-100	$\dot{m}_{13}h_{13} + \dot{W} = \dot{m}_{14}h_{14}$
E−101	$\dot{m}_{16}h_{16} + \dot{m}_{20}h_{20} = \dot{m}_{17}h_{17} + \dot{m}_{34}h_{34}$
C-100	$\dot{m}_{18}h_{18} + \dot{Q}_R = \dot{m}_{19}h_{19} + \dot{m}_{20}h_{20}$
E−103	$\dot{m}_{15}h_{15} + \dot{m}_{19}h_{19} = \dot{m}_{22}h_{22} + \dot{m}_{23}h_{23}$
VLV-100	$\dot{m}_{34}h_{34} = \dot{m}_{35}h_{35}$
E−106	$\dot{m}_{36}h_{36} = \dot{Q} + \dot{m}_{37}h_{37}$
E−104	$\dot{m}_{21}h_{21} + \dot{m}_{24}h_{24} = \dot{m}_{28}h_{28} + \dot{m}_{29}h_{29}$
T-101	$\dot{m}_{28}h_{28} = \dot{W} + \dot{m}_{30}h_{30}$
E−105	$\dot{m}_{30}h_{30} + \dot{m}_{31}h_{31} = \dot{m}_{32}h_{32} + \dot{m}_{33}h_{33}$
E−107	$\dot{m}_{29}h_{29} + \dot{m}_{39}h_{39} = \dot{m}_{40}h_{40} + \dot{m}_{38}h_{38}$

$$\sum \dot{m}_i h_i - \sum \dot{m}_o h_o = \dot{W} - \dot{Q} \tag{9}$$

The general equation for calculating the efficiency of the first law of thermodynamics (energy efficiency (ω_{en}), electrical efficiency (ω_{el}), and CHP efficiency (ω_{CHP}) is defined in Eq. (10) to Eq. (12). Additionally, based on these equations, they are rewritten explicitly for the proposed system (Fig. 3) in Table 6. The heating value of fuel (tars) is equal to 5734 kJ/kg, and the heating value of hydrogen is equivalent to 119900 kJ/kg.

$$\omega_{en} = \frac{\dot{W}_{net} + \dot{Q}_{heating} + \dot{Q}_{cooling} + \text{Hydrogen energy}}{\dot{m}_{fuel}LHV_{fuel}} \tag{10}$$

$$\omega_{el} = \frac{\dot{W}_{net}}{\dot{m}_{fuel}LHV_{fuel}} = \frac{\sum \dot{W}_{turbine} - \sum \dot{W}_{pump} - \dot{W}_{PEM} - \dot{W}_{compressor}}{\dot{m}_{fuel}LHV_{fuel}} \tag{11}$$

$$\omega_{CHP} = \frac{\dot{W}_{net} + \dot{Q}_{heating}}{\dot{m}_{fuel}LHV_{fuel}} \tag{12}$$

Fig. 4 clearly shows the energy flow status for the main subsystems, and the input and output energies are also specified. According to Fig. 4, the TCS subsystem's total input energy includes tars' chemical energy ($\dot{m}_1 LHV_1$) and the consumed power of the K-100 compressor. The total input energy to the TCS subsystem is 1170503.98 kW. This is while the product of this subsystem is hot water, which is produced through the E−112 heat exchanger, and the heating value ($\dot{m}_{62} \times [h_{63} - h_{62}]$)) is 11650 kW. Therefore, according to Fig. 4 and the equations mentioned in Table 6, the energy efficiency of the TCS subsystem is equal to 1%.

Regarding the LGTS subsystem, all the input energy comes from the difference in energy for the hot flue gas ($\dot{m}_5 \times [h_5 - h_7]$). It shares this energy with the octane working fluid in the E−100 heat exchanger (1196740 kW) and generates heat and power. The heat produced in this subsystem is through the E−109 ($\dot{m}_{48} \times [h_{49} - h_{48}]$), and E−111 ($\dot{m}_{57} \times [h_{57} - h_{56}]$) heat exchangers and the total amount of heat produced is equal to 608600 kW by Fig. 4. According to Fig. 4, the total net power ($\dot{W}_{T100} - \dot{W}_{P101} - \dot{W}_{P102} + \dot{W}_{T102} + \dot{W}_{T103} - \dot{W}_{P103}$) generated in this section is also equivalent to 306197.9 kW. Therefore, this part's energy and electrical efficiencies are 76.42% and 25.58%, respectively. After hot water production, the flue gas is released by leaving the LGTS subsystem. On the other hand, hot octane working fluid is used to supply the driving force in the GUS section. As shown in Fig. 4, the total input energy through this way ($\dot{m}_{11} \times [h_{11} - h_{38}]$) is equal to 281912.4 kW. The products of this subsystem include heating from the E−107 heat exchanger ($\dot{m}_{40} \times [h_{40} - h_{39}]$), cooling from the E−105 heat exchanger ($\dot{m}_{31} \times [h_{31} - h_{32}]$), and generating net power ($\dot{W}_{T101} - \dot{W}_{P100}$). The values of these products are shown in Fig. 4. Therefore, the electrical and energy efficiencies in this section are 6.86% and 49.25%, respectively. According to the Aspen HYSYS flow sheet, 23.9% of the gross production power ($\sum \dot{W}_{turbine}$) should be sent to CRV-01 to produce hydrogen through the PEM electrolyzer. In this way, hydrogen can be produced with an energy of 67150 kW. Therefore, the energy efficiency of the HPS section is 84.24%. In Fig. 5, the electrical and energy efficiencies for all the subsystems have been compared.

According to this study, in organic Rankine cycles with heptane (ORC-C7) and pentane (ORC-C5) working fluids, the energy efficiency reaches 99.97%, which allocates the highest value. This is due to the production of heating products in E−109 and E−111 heat exchangers and the net power in these two cycles, which maximizes the utilization of input energy. According to Fig. 5, based on the first law of thermodynamics, the minimum and maximum efficiencies are for the TCS subsystem (1%) and ORC-C7 and ORC-C5 cycles (97/99%), respectively. Additionally, among power generation subsystems, the highest efficiency is obtained by LGTS (25.58%). Finally, based on Fig. 4 and the equations presented in Table 6, the overall energy, electrical, and CHP efficiencies for the new process are 89.72%, 19.37%, and 83.62%, respectively. The energy and CHP efficiencies are compared with other articles in Tables 7 and 8, and improvements are reported. According to the comparisons, the proposed system has high power and performs better than a wide range of similar systems, which is apparent through the improved percentage values.

4.2. Exergy analysis

Energy is transformed during a process and according to the first law of thermodynamics, it is not possible to analyze its consumption quality accurately for a specific point (Cao et al., 2020). Therefore, exergy analysis is highly necessary and examines the energy utilization efficiency for each point or equipment.

Therefore, the exergy account, employing the principles of the second law of thermodynamics, yields the following equations for the exergy destruction of each component:

Table 6
Equations related to the energy, electrical, and CHP efficiency of the proposed system.

Units	Equations
TCS	$\omega_{en} = \frac{\dot{m}_{62} \times [h_{63} - h_{62}]}{\dot{m}_1 LHV_1 + \dot{W}_{K100}}$
LGTS	$\omega_{en} = \frac{\dot{W}_{T100} - \dot{W}_{P101} - \dot{W}_{P102} + \dot{W}_{T102} + \dot{W}_{T103} - \dot{W}_{P103} + \dot{m}_{48} \times [h_{49} - h_{48}] + \dot{m}_{57} \times [h_{57} - h_{56}]}{\dot{m}_5 \times [h_5 - h_7]}$
LGTS	$\omega_{el} = \frac{\dot{W}_{T100} - \dot{W}_{P101} - \dot{W}_{P102} + \dot{W}_{T102} + \dot{W}_{T103} - \dot{W}_{P103}}{\dot{m}_5 \times [h_5 - h_7]}$
ORC-C8	$\omega_{el} = \omega_{en} = \frac{\dot{W}_{T100} - \dot{W}_{P103}}{\dot{m}_5 \times [h_5 - h_7]}$
ORC-C7	$\omega_{en} = \frac{\dot{W}_{T102} - \dot{W}_{P101} + \dot{m}_{48} \times [h_{49} - h_{48}]}{\dot{m}_{41} \times [h_{41} - h_{43}]}$
ORC-C7	$\omega_{el} = \frac{\dot{W}_{T102} - \dot{W}_{P101}}{\dot{m}_{41} \times [h_{41} - h_{43}]}$
ORC-C5	$\omega_{en} = \frac{\dot{W}_{T103} - \dot{W}_{P102} + \dot{m}_{57} \times [h_{57} - h_{56}]}{\dot{m}_{42} \times [h_{42} - h_{51}]}$
ORC-C5	$\omega_{el} = \frac{\dot{W}_{T103} - \dot{W}_{P102}}{\dot{m}_{42} \times [h_{42} - h_{51}]}$
GUS	$\omega_{el} = \frac{\dot{W}_{T101} - \dot{W}_{P100}}{\dot{m}_{11} \times [h_{11} - h_{38}]}$
GUS	$\omega_{en} = \frac{\dot{W}_{T101} - \dot{W}_{P100} + \dot{m}_{31} \times [h_{31} - h_{32}] + \dot{m}_{40} \times [h_{40} - h_{39}]}{\dot{m}_{11} \times [h_{11} - h_{38}]}$
HPS	$\omega_{en} = \frac{\dot{m}_{71} LHV_{71}}{\dot{W}_{CRV101} + \dot{W}_{P104}}$
Overall	$\omega_{en} = \frac{\dot{W}_{net} + \dot{m}_{48} \times [h_{49} - h_{48}] + \dot{m}_{57} \times [h_{57} - h_{56}] + \dot{m}_{31} \times [h_{31} - h_{32}] + \dot{m}_{40} \times [h_{40} - h_{39}] + \dot{m}_{71} LHV_{71} + \dot{m}_{62} \times [h_{63} - h_{62}]}{\dot{m}_1 LHV_1}$
Overall	$\omega_{el} = \frac{\dot{W}_{net}}{\dot{m}_1 LHV_1}$
Overall	$\omega_{CHP} = \frac{\dot{W}_{net} + \dot{m}_{48} \times [h_{49} - h_{48}] + \dot{m}_{57} \times [h_{57} - h_{56}] + \dot{m}_{62} \times [h_{63} - h_{62}] + \dot{m}_{40} \times [h_{40} - h_{39}]}{\dot{m}_{11} \times [h_{11} - h_{38}]}$

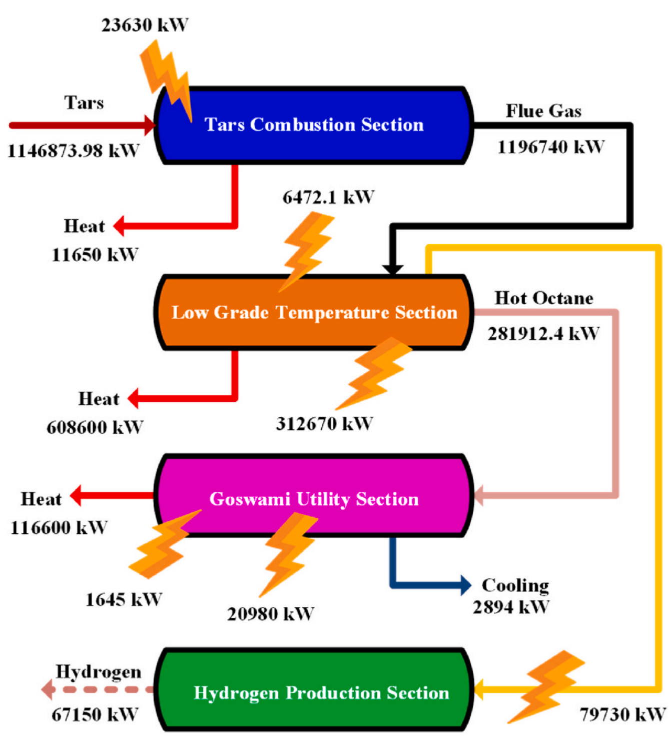

Fig. 4. Energy flow diagram for proposed process.

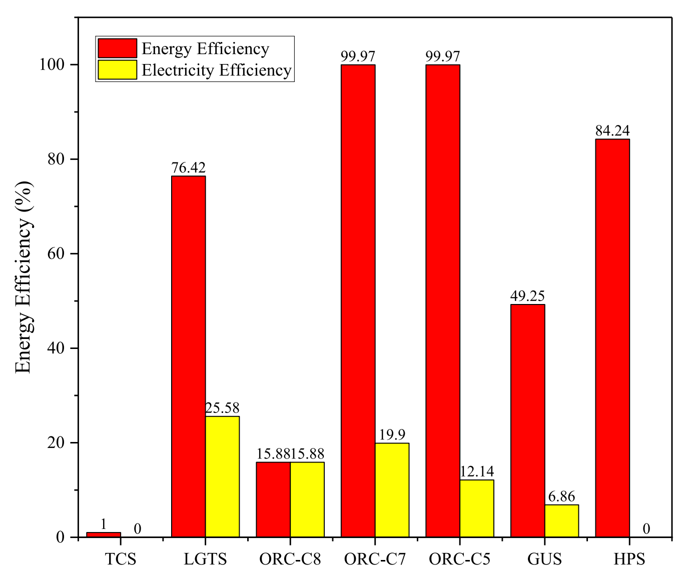

Fig. 5. Comparison of energy and electrical efficiencies for subsystems of the proposed process.

$$\dot{E}_{x,dest} = \sum_j \left(1 - \frac{T_0}{T_j}\right)\dot{Q}_j - \dot{W}_{cw,k} + \sum_i \dot{E}_{x,in} - \sum_e \dot{E}_{x,out} = \dot{E}_{x,F} - \dot{E}_{x,P} \quad (13)$$

where $\dot{E}_{x,dest}$ is the exergy destruction rate depending on the exergy rate of heat transfer ($\sum_j \left(1 - \frac{T_0}{T_j}\right)\dot{Q}_j$), exergy rate of power ($\dot{W}_{cw,k}$), and input and output exergy rates of streams ($\sum_i \dot{E}_{in} - \sum_e \dot{E}_{out}$). Also, $\dot{E}_{x,dest}$ is defined as the difference between fuel exergy rate ($\dot{E}_{x,F}$) and product exergy rate ($\dot{E}_{x,P}$).

The exergy of a stream is composed of physical (e_{ph}) and chemical (e^{ch}) exergy (Eq. (14) and Eq. (15)) (Dincer and Rosen, 2012; Moran and

Table 7
Comparison of energy efficiency with other studies.

Studies	Process	ω_{en} [%]	Improved (%)
Ref (Suleman et al., 2014)	Renewable energy system for multi-generation	54.7	35.02
Ref (X. Liu et al., 2023b)	Multigeneration system using a combined power plant based on geothermal energy and oxyfuel combustion	47.2	42.52
Ref (X. Liu et al., 2023a)	Trigeneration system	66.9	22.82
Ref (Razeghi et al., 2014)	Biogas trigeneration system with fuel cells	87.5	2.22
Ref (Gu et al., 2023)	Electricity and methanol co-generation using heat recovery	64.13	25.59
Ref (Khalid et al., 2016)	Multigeneration system for green buildings	46.1	43.62
Ref (Zhu et al., 2018)	Synthetic natural gas and power polygeneration	58.84	30.88
Ref (Ansari et al., 2021)	Multigeneration system using geothermal energy	49.1	40.62
Ref (Akrami et al., 2018)	Multigeneration energy system	33.9	55.82
Ref (Islam et al., 2018)	Solar energy based multigeneration system with thermoelectric generator	59.6	30.12
Ref (Bellos and Tzivanidis, 2018)	Solar-driven trigeneration system	87.39	2.33
Ref (Y. Li et al., 2014)	Polygeneration system based on partial gasification	51.16	38.56
Ref (J. Fan et al., 2017)	Polygeneration system based on Coal	60.34	29.38
Current study	Polygeneration system based on Tars Combustion	**89.72**	–

Table 8
Comparison of CHP efficiency with other systems.

Studies	process	ω_{CHP} [%]	Improved (%)
Ref (P. Ahmadi et al., 2011)	Trigeneration energy system	76.76	6.86
Ref (MosayebNezhad et al., 2019)	Biogas trigeneration system with microturbines	81.2	2.42
Ref (Guo et al., 2020)	Solid oxide fuel cell-gas turbine cogeneration system	64.4	19.22
Ref (Cao et al., 2021)	SCO_2 cycle, gasifier, combustion chamber, and a domestic water heater	75.89	7.73
Ref (Ji-chao & Sobhani, 2021)	A gas turbine cycle, a supercritical CO2 cycle, and a Kalina cycle	78.15	5.47
Ref (Ehyaei and Rosen, 2019)	Solid oxide fuel cell and gas and steam cycles	60	23.62
Current study	Polygeneration system based on Tars Combustion	83.62	–

Tsatsaronis, 2017).

$$e_{ph} = [h - h_0] - T_0[s - s_0] \tag{14}$$

$$e^{ch} = \sum \varkappa_i e_i^0 + RT_0 \sum \varkappa_i \ln \varkappa_i \delta_i \tag{15}$$

where T_0 is the reference temperature, h is the enthalpy of the stream, s is the entropy, h_0 is the enthalpy in standard conditions, and δ is the activity coefficient. In addition, ϰ represents the mole fraction for each component used in the proposed process.

Moreover, for each subsystem and the entire process, the second law efficiency (Ψ_{ex}) is calculated using Eq. (16) (Gu et al., 2023). Furthermore, the share of exergy destruction for each component is obtained from Eq. (17) (Chitsaz et al., 2019; Yu et al., 2023).

$$\Psi_{ex} = \frac{\dot{E}_{x,P}}{\dot{E}_{x,F}} = 1 - \frac{\dot{E}_{x,dest}}{\dot{E}_{x,F}} \tag{16}$$

$$\beta_{Dest} = \frac{\dot{E}^{i}_{x,dest}}{\sum \dot{E}_{x,dest}} \tag{17}$$

The exergy destruction equations for the equipment used in the proposed process are listed in Table 9. Moreover, the second law efficiency is presented for subsystems and the entire proposed process in Table 10. In these equations, T_H is the temperature of hot water, which is equal to 323.15 K, and T_C is also the temperature of cold water and is equivalent to 278.15 K.

The exergy flow diagram for the proposed process (Fig. 3) is shown in Fig. 6. Based on this figure, the total available exergy in the TCS subsystem is equal to the exergy of the tars stream (stream 1), which has a value of 640856.65 kW (the available exergy for the entire process is also included). In this subsystem, the total exergy of the product is equal to the value of $\dot{Q}_{E112} \times \left[1 - \frac{T_0}{T_H}\right]$, which according to Fig. 6, equals 901.28 kW. Therefore, the exergy efficiency equals 0.13%, indicating that this part has the lowest exergy efficiency. However, the flue gas stream exiting from the CRV-100 provides exergy to the LGTS section, which according to Fig. 6, has a value of 848154 kW. In this subsystem, the total produced exergy is initially equal to the net power plus the exergy resulting from the production of hot water from heat exchangers E−109 ($\dot{Q}_{E109} \times \left[1 - \frac{T_0}{T_H}\right]$ and E−111 ($\dot{Q}_{E111} \times \left[1 - \frac{T_0}{T_H}\right]$). Therefore, the exergy efficiency in this subsystem will be 41.65%. The hot octane fluid that exits the T-100 expansion turbine is the driving force in the ORC and GUS subsystems. In the GUS subsystem, the value of the available exergy, according to Fig. 6, is equal to 85113.75 kW. On the other hand, the total exergy of the product includes the cold-water exergy ($\dot{Q}_{E105} \times$

Table 9
Exergy destruction equations for the components of the proposed process.

Components	Equations
K-100	$\dot{E}_2 + \dot{W} - \dot{E}_3$
CRV-100	$\dot{E}_4 - \dot{E}_5$
E−100	$\dot{E}_5 + \dot{E}_8 - \dot{E}_9 - \dot{E}_7$
T-100	$\dot{E}_9 - \dot{E}_{10} - \dot{W}$
E−112	$\dot{E}_7 + \dot{E}_{62} - \dot{E}_{63} - \dot{E}_{61}$
P-104	$\dot{E}_{67} + \dot{W} - \dot{E}_{70}$
CRV-101	$\dot{E}_{70} + \dot{W} - \dot{E}_{68} - \dot{E}_{69}$
X-100	$\dot{E}_{68} + \dot{E}_{69} - \dot{E}_{71} - \dot{E}_{72}$
X-101	$\dot{E}_{72} - \dot{E}_{73} - \dot{E}_{74}$
E−113	$\dot{E}_{74} - \dot{E}_{75}$
E−108	$\dot{E}_{41} + \dot{E}_{44} - \dot{E}_{43} - \dot{E}_{45}$
T-102	$\dot{E}_{45} - \dot{E}_{46} - \dot{W}$
E−109	$\dot{E}_{48} + \dot{E}_{46} - \dot{E}_{49} - \dot{E}_{47}$
P-101	$\dot{E}_{47} + \dot{W} - \dot{E}_{50}$
E−110	$\dot{E}_{42} + \dot{E}_{52} - \dot{E}_{51} - \dot{E}_{53}$
T-103	$\dot{E}_{53} - \dot{W} - \dot{E}_{54}$
E−111	$\dot{E}_{56} + \dot{E}_{54} - \dot{E}_{55} - \dot{E}_{57}$
P-102	$\dot{E}_{55} + \dot{W} - \dot{E}_{58}$
P-103	$\dot{E}_{59} + \dot{W} - \dot{E}_{60}$
P-100	$\dot{E}_{13} + \dot{W} - \dot{E}_{14}$
E−101	$\dot{E}_{16} + \dot{E}_{20} - \dot{E}_{17} - \dot{E}_{34}$
C-100	$\dot{E}_{18} + \dot{Q}_R\left(1 - \frac{T_0}{T_R}\right) - \dot{E}_{19} - \dot{E}_{20}$
E−103	$\dot{E}_{15} + \dot{E}_{19} - \dot{E}_{22} - \dot{E}_{23}$
VLV-100	$\dot{E}_{34} - \dot{E}_{35}$
E−106	$\dot{E}_{36} - \dot{E}_{37}$
E−104	$\dot{E}_{21} + \dot{E}_{24} - \dot{E}_{28} - \dot{E}_{29}$
T-101	$\dot{E}_{28} - \dot{W} - \dot{E}_{30}$
E−105	$\dot{E}_{30} + \dot{E}_{31} - \dot{E}_{32} - \dot{E}_{33}$
E−107	$\dot{E}_{29} + \dot{E}_{39} - \dot{E}_{40} - \dot{E}_{38}$

Table 10
Exergy efficiency equations for subsystems and the entire proposed process.

Units	Equations
TCS	$\Psi_{ex} = \frac{\dot{Q}_{E112} \times \left[1-\frac{T_0}{T_H}\right]}{\dot{E}_1^{PH}+\dot{E}_1^{CH}+\dot{W}_{K100}}$
LGTS	$\Psi_{ex} = \frac{\dot{W}_{T100}-\dot{W}_{P101}-\dot{W}_{P102}+\dot{W}_{T102}+\dot{W}_{T103}-\dot{W}_{P103}+\dot{Q}_{E109} \times \left[1-\frac{T_0}{T_H}\right]+\dot{Q}_{E111} \times \left[1-\frac{T_0}{T_H}\right]}{\dot{E}_5-\dot{E}_7}$
ORC-C_8	$\Psi_{ex} = \frac{\dot{W}_{T100}-\dot{W}_{P103}+\dot{Q}_{E109} \times \left[1-\frac{T_0}{T_H}\right]}{\dot{E}_5-\dot{E}_7}$
ORC-C_7	$\Psi_{ex} = \frac{\dot{W}_{T102}-\dot{W}_{P101}+\dot{Q}_{E109} \times \left[1-\frac{T_0}{T_H}\right]}{\left[\dot{E}_{41}-\dot{E}_{43}\right]}$
ORC-C_5	$\Psi_{ex} = \frac{\dot{W}_{T103}-\dot{W}_{P102}+\dot{Q}_{E111} \times \left[1-\frac{T_0}{T_H}\right]}{\left[\dot{E}_{42}-\dot{E}_{51}\right]}$
GUS	$\Psi_{ex} = \frac{\dot{W}_{T101}-\dot{W}_{P100}+\dot{Q}_{E105} \times \left[\frac{T_0}{T_C}-1\right]+\dot{Q}_{E107} \times \left[1-\frac{T_0}{T_H}\right]}{\left[\dot{E}_{11}-\dot{E}_{38}\right]}$
HPS	$\Psi_{ex} = \frac{\dot{E}_{71}^{PH}+\dot{E}_{71}^{CH}}{\dot{W}_{CRV101}+\dot{W}_{P104}}$
Overall	$\Psi_{ex} = \frac{\dot{W}_{net}+\dot{Q}_{E109} \times \left[1-\frac{T_0}{T_H}\right]+\dot{Q}_{E111} \times \left[1-\frac{T_0}{T_H}\right]+\dot{Q}_{E105} \times \left[\frac{T_0}{T_C}-1\right]+\dot{Q}_{E107} \times \left[1-\frac{T_0}{T_H}\right]+\dot{E}_{71}^{PH}+\dot{E}_{71}^{CH}+\dot{Q}_{E112} \times \left[1-\frac{T_0}{T_H}\right]}{\dot{E}_1^{PH}+\dot{E}_1^{CH}}$

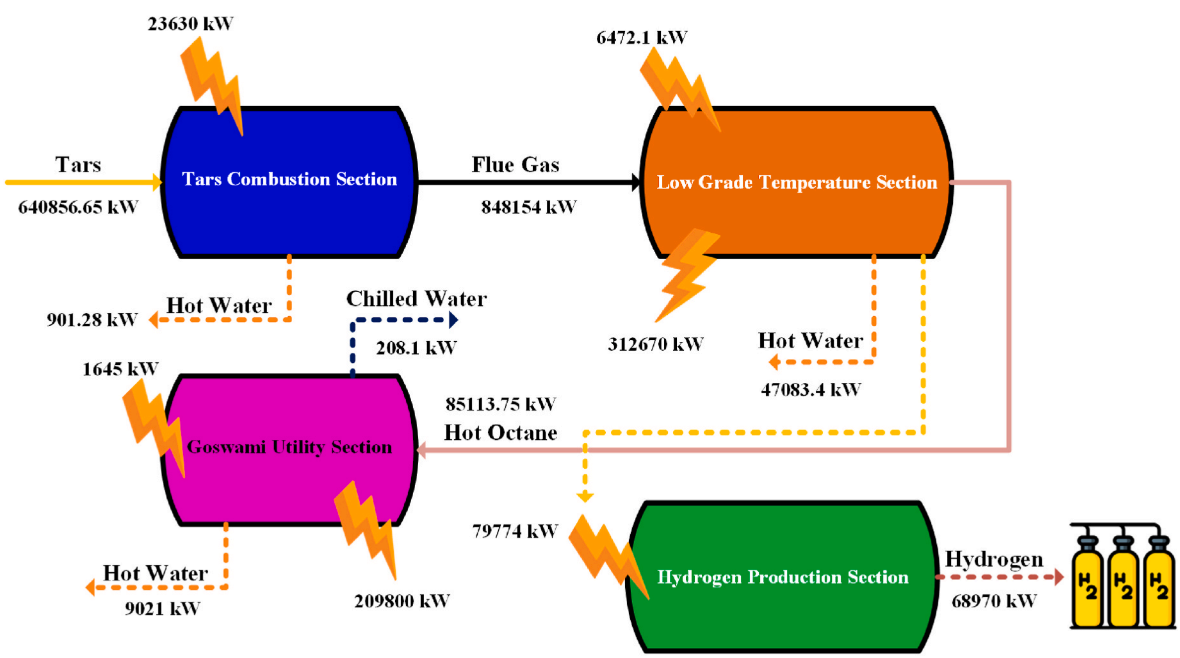

Fig. 6. Exergy flow diagram for the proposed polygeneration process.

$\left[\frac{T_0}{T_C}-1\right]$), the hot water exergy ($\dot{Q}_{E107} \times \left[1-\frac{T_0}{T_H}\right]$), and the net power, which has a total amount of 28564.1 kW. Therefore, the second law efficiency equals 36.96% for the GUS subsystem.

Regarding the HPS subsystem, the total available exergy is equivalent to all power supplied to the electrolyzer and P-104 pump, which according to Fig. 6, has a value of 79774 kW. The total exergy of the product is also equal to the exergy of the hydrogen stream. However, the exergy efficiency for the HPS subsystem has been evaluated as 86.46%. The LGTS subsystem is composed initially of three organic Rankine cycles, and the efficiency of each one is presented separately in Table 10. According to Fig. 7, the organic Rankine cycle with heptane as the working fluid has achieved the highest efficiency among the other two ORCs. This indicates that even in terms of efficiency (86.41%), the heptane cycle is able to compete with the HPS cycle, whose exergy product is chemical. However, the use of E−109 and E−111 heat exchangers, which have been used for heat recovery, has a significant impact on increasing exergy efficiency. The ORC cycle with pentane as the working fluid also shows excellent efficiency (62.73%). According to Fig. 6, in the proposed process, the total available exergy (stream 1) and the total product exergy are equal to 640856.65 kW and 348300 kW, respectively. Therefore, its exergy efficiency is equivalent to 54.35%, which has been compared with previous studies in Table 11. According to Table 11, the proposed process has a better thermodynamic performance than similar systems using different energy sources (renewable, biomass, fuel cell, etc). This is due to the widespread use of heat recovery exchangers in the entire polygeneration structure.

The results of exergy destruction calculations for the equipment used in the proposed system are reported in Table 12. According to the calculations, the process's total irreversibility equals 859,492 kW. The

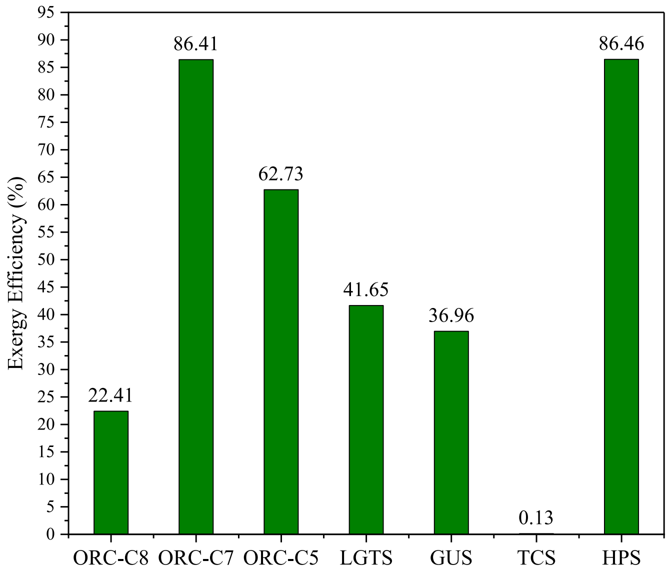

Fig. 7. Comparison of exergy efficiency for subsystems of the proposed process.

Table 11
Comparison of exergy efficiency with other papers.

Studies	Process	Ψ_{ex}[%]	Improved (%)
Ref (P. Ahmadi et al., 2013)	Integrated biomass-based multi-generation energy system	22.2	32.15
Ref (G. Fan et al., 2021)	Polygeneration system integrated gas cycle, absorption chiller, and Copper–Chlorine thermochemical cycle	44	10.35
Ref (J. Wang and Yang, 2016)	Polygeneration based on biomass and solar energy	16.1	38.25
Ref (Jana and De, 2015)	Polygeneration using agricultural waste	47.5	6.85
Ref (Rian & Ertesvåg, 2012)	Combined heat and power systems	43.5	10.85
Ref (S. Ahmadi et al., 2019)	Fuel cell-based CHP	49.58	4.77
Ref (Siddiqui et al., 2019)	Geothermal-based trigeneration system	35.9	18.45
Current study	Polygeneration system based on Tars Combustion	54.35	–

LGTS subsystem has the largest share of exergy destruction (72%). In contrast, the HPS subsystem has the lowest destruction (according to Fig. 8). Additionally, the results in Table 12 indicate that in the entire proposed process, the E−100 heat exchanger in the LGTS subsystem has the highest share of irreversibility with exergy destruction of 348,051 kW (40.49%). The exergy efficiency of this heat exchanger is 58.96% according to the general Eq. (16), indicating a 41.04% exergy destruction in this part of the process. The low exergy efficiency in this evaporator is the main factor for the lower exergy efficiency of the organic Rankine cycle with octane working fluid compared to the other two organic cycles. According to Table 12, the exergy efficiencies of E−108 and E−110 evaporators are 92% and 61.05%, respectively, which are much higher than the E−100 evaporator in the ORC cycle with octane working fluid.

4.3. Environmental analysis

The analysis of CO_2 is of utmost importance within the energy system, as it comprehensively elucidates and addresses the environmental

Table 12
Calculation results of exergy destruction rate for equipment and subsystems of the proposed process.

Tars Combustion Section			
Components	$\dot{E}_{x,in}(kW)$	$\dot{E}_{x,out}(kW)$	$\dot{E}_{x,D}(kW)$
K-100	23630	21698	1932
CRV-100	1167968	985156	182812
E−112	1813	369	1444
	1193411	1007223	186188
Low-Grade Temperature Section			
Components	$\dot{E}_{x,in}(kW)$	$\dot{E}_{x,out}(kW)$	$\dot{E}_{x,D}(lW)$
E−100	848154	500103	348051
T-100	516987	511610	5377
E−108	109440	100690	8750
T-102	101458	90911	192369
E−109	17751	9360	8391
P-101	1055	768	287
E−110	109440	66818	42622
T-103	67635	60667	6968
E−111	15568	10826	4742
P-102	1088	816	272
P-103	17749	17440	309
	1806325	1188187	618138
Goswami Utility Section			
Components	$\dot{E}_{x,in}(kW)$	$\dot{E}_{x,out}(kW)$	$\dot{E}_{x,D}(kW)$
C-100	75918	68873	7045
E−107	20036	3966	16070
E−101	26228	20221	6007
P-100	12920	12545	375
E−103	8930	2503	6427
S-100	37381	37312	69
E−106	11000	6200	4800
E−104	860	743	117
T-101	37264	26072	11192
E−105	181	102	79
	230718	178537	52181
Hydrogen Production Section			
Components	$\dot{E}_{x,in}(kW)$	$\dot{E}_{x,out}(kW)$	$\dot{E}_{x,D}(kW)$
P-104	94	89	5
CRV-101	79730	76845	2885
X-100	4171	4114	57
X-101	1398	1370	28
E−113	41	31	10
	85434	82449	2985

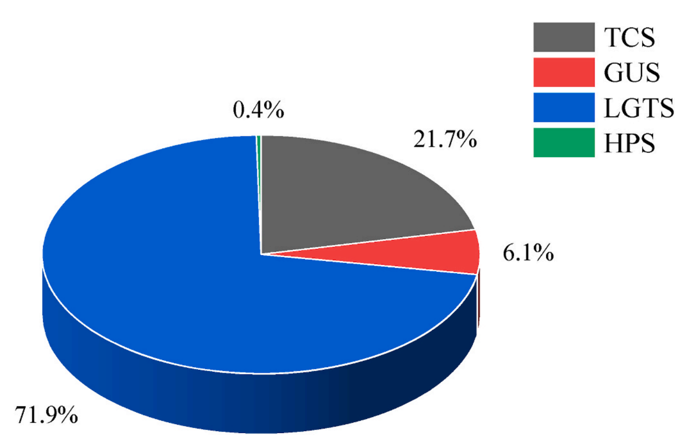

Fig. 8. Comparing the share of exergy destruction for the subsystems of the proposed process.

repercussions inherent in both the production and consumption of energy resources. Through the comprehensive examination of CO_2 emissions associated with diverse sources, including power plants, transportation systems, and industrial sectors, policymakers, and energy strategists can effectively devise and implement measures to mitigate greenhouse gas release (Y. Y. Wang et al., 2022). This analysis enables the identification of sectors that emit significant amounts of greenhouse gases and facilitates the adoption of specific strategies to transition toward cleaner and more sustainable energy sources (Haghghi et al., 2023). Furthermore, CO_2 analysis plays a crucial role in monitoring advancements toward climate targets and assessing the efficacy of energy policies and technologies in mitigating carbon emissions. Consequently, the evaluation of CO_2 emissions serves to enable well-informed decision-making (L. Liu et al., 2022). It appropriately supports transitioning towards a more environmentally sustainable energy system with a reduced carbon footprint (Miao et al., 2020). Hence, one important and competitive parameter for multi-generation systems is determining or calculating the intensity of CO_2 emissions (specific CO_2 emission, SCE). This parameter is defined based on Eq. (18) (P. Ahmadi et al., 2013).

$$\in_{CO_2}\left(\frac{kg}{kWh}\right)=\frac{\dot{m}_{CO_2}}{\dot{Q}_{heating}+\dot{Q}_{cooling}+\dot{W}_{net}+\dot{E}_{heating}+\dot{E}_{cooling}+\dot{E}_{H_2}} \tag{18}$$

In Eq. (18), the parameter $\dot{m}_{CO_2}$ refers to the difference in the CO_2 flow rate between the flue gas stream and the input tar (stream 1 in Fig. 3). Therefore, $\dot{m}_{CO_2}$ is referred to as net emission intensity (Eq. (19)):

$$\dot{m}_{CO_2}\left(\frac{kg}{h}\right)=\dot{m}_{CO_2}^{flue\ gas}-\dot{m}_{CO_2}^{Tar} \tag{19}$$

The CO_2 flow diagram is shown in Fig. 9. Based on this figure, 198267.56 kg/h of CO_2 is introduced into the process through the tar stream, which is the fuel of the process and the system has no role in its creation. On the other hand, after the combustion of the fuel in CRV-100, the amount of CO_2 in the flue gas reaches 452257.36 kg/h. According to Fig. 9, this flue gas stream passes through the LGTS subsystem and is released. In other parts of the proposed process, due to heat integration and heat recovery in heat exchanger networks, no other emissions (indirect emissions) occur. Therefore, according to Eq. (19), the net CO_2 emission rate ($\dot{m}_{CO_2}$) is equivalent to 253989.8 kg/h. Thus, based on Eq. (18) and the values of energy and exergy products obtained in the thermodynamic evaluation section, the SCE parameter ($\in_{CO_2}$) for this new process has been evaluated as 0.22 kg/kWh. The overall results of the environmental assessment are listed in Table 13.

In the previous section, by comparing the parameter $\in_{CO_2}$ to other studies, the amount of CO_2 emissions reduction is calculated and reported in Table 14. In this section, the aim is to calculate the reduction value of CO_2 emissions ($\mu^*_{CO_2}$) through the proposed process (Fig. 3)

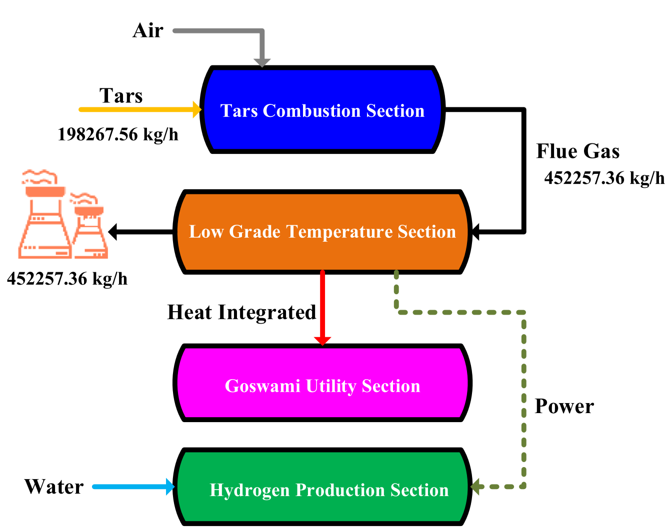

Fig. 9. CO_2 flow diagram for the proposed process.

Table 13
Overall results for environmental assessment.

Parameter	Value
Indirect emission (kg/h)	0.0
direct emission (kg/h)	452257.36
CO_2 in fuel (kg/h)	198267.56
Net CO_2 emission (kg/h)	253989.8
Specific CO_2 emission (kg/kWh)	0.22

Table 14
Comparison of CO_2 footprint with other papers.

Studies	Process	$\in_{CO_2}$ (kg /kWh)	Reduction (%)
Ref (P. Ahmadi et al., 2013)	Integrated biomass-based multi-generation energy system	0.519	57.61
Ref (D. Wang et al., 2023b)	Cogeneration plant with integration of biomass and geothermal energies	0.744	70.43
Ref (Mohammadi et al., 2020)	Solar-driven trigeneration system	0.24	8.33
Ref (Auñón-Hidalgo et al., 2021)	Combined solar photovoltaic and thermal, with a Stirling engine-based micro-CHP system	0.267	17.6
Current study	Polygeneration system based on Tars	0.22	–

compared to reference articles (P. Ahmadi et al., 2013; Auñón-Hidalgo et al., 2021; Mohammadi et al., 2020; D. Wang et al., 2023b) according to Eq. (20). In Eq. (20), the parameter $\Delta\in_{CO_2}$ represents the difference of the parameter $\in_{CO_2}$ between reference articles (P. Ahmadi et al., 2013; Auñón-Hidalgo et al., 2021; Mohammadi et al., 2020; D. Wang et al., 2023b) and the proposed process.

$$\mu^*_{CO_2}\left(\frac{kg}{h}\right)=\Delta\in_{CO_2}\times\left[\dot{Q}_{heating}+\dot{Q}_{cooling}+\dot{W}_{net}+\dot{E}_{heating}+\dot{E}_{cooling}+\dot{E}_{H_2}\right] \tag{20}$$

According to Eq. (20), in Table 15, the values of the parameter $\mu^*_{CO_2}$ are reported compared to other studies.

4.4. Economic analysis

This article has conducted a comprehensive economic analysis of the proposed system. For this purpose, Table 16 has been used to calculate the total capital investment cost (TCI). Where Z_{total} represents the total cost of equipment used in the process. The purchase cost of each component is given in Table 17.

Based on two parameters, the total energy cost and fixed investment cost (C), the total annual cost (TAC) is calculated using Eq. (21) (Ansari et al., 2021), assuming an interest rate (l) of 14% and a system lifetime (s) of 20 years (Cao et al., 2021). The fuel used in the new process is a

Table 15
The results of calculating the parameter $\mu^*_{CO_2}$ compared to other studies.

Process	$\Delta\in_{CO_2}\left(kg/h\right)$	$\mu^*_{CO_2}\left(kg/h\right)$
Integrated biomass-based multi-generation energy system (P. Ahmadi et al., 2013)	0.299	345345
Cogeneration plant with integration of biomass and geothermal energies (D. Wang et al., 2023b)	0.524	605220
Solar-driven trigeneration system (Mohammadi et al., 2020)	0.02	23100
Combined solar photovoltaic and thermal, with a Stirling engine (Diesel oil) micro-CHP system (Auñón-Hidalgo et al., 2021)	0.047	54285

Table 16
The parameters for estimating the total capital investment cost.

Parameters	
Purchased-Equipment Cost	Z_{total}
Purchased-Equipment installation	$0.9\ Z_{total}$
Piping	$0.7\ Z_{total}$
Instrumentation and Controls	$0.4\ Z_{total}$
Electrical Equipment and Materials	$0.15\ Z_{total}$
Land	$0.1\ Z_{total}$
Civil, Structural, and Architectural Work	$0.9\ Z_{total}$
Service Facilities	Z_{total}
Total Direct Costs (A)	$5.15\ Z_{total}$
Engineering and Supervision	$0.75\ Z_{total}$
Construction Costs	$0.15 \times A$
Contingencies	$0.25 \times (0.75\ Z_{total} + 0.15A)$
Total Indirect Costs (B)	$1.903\ Z_{total}$
Total Fixed Capital Investment (C)	$7.053\ Z_{total}$
Startup Costs	$0.85\ Z_{total}$
Working Capital	$0.2\ D$
Allowance for Funds Used During Construction	$0.15 \times C$
Total Capital Investment (D)	$1.33 \times C$

Table 17
The equations related to estimating the cost of equipment.

Components	Equation
Turbine (Ghorbani et al., 2020)	$6000 \times \dot{W}^{0.7}$
Pump (Ghorbani et al., 2020)	$3540 \times \dot{W}^{0.71}$
Valve (Javadi et al., 2021)	$114 \times \dot{m}_i \left(\frac{kg}{s}\right)$
Separator (H. Wei et al., 2023)	$17640 \times D^{1.06}(m) \times L^{0.802}(m)$
Compressor (Sadat et al., 2020)	$91562 \times \left[\frac{\dot{W}}{455}\right]^{0.67}$
PEM (Bellotti et al., 2017)	$1500 \times \dot{W}_{stack}^{0.85}$
ORC (Petrecca, 2014)	$3464 \times \dot{W} / \dot{W}^{0.357}$
Chamber (Sadat et al., 2020)	$46.08 \times \frac{[1 + \exp(0.018T_{72} - 26.4)]}{0.995 - \frac{p_{in}}{p_{out}}} \times \dot{m}_i$
Exchanger (Kianfard et al., 2018)	$309.14 \times A^{0.85}$

byproduct of biomass gasification processing. Therefore, the energy cost is related to the cost of providing cooling water utility (H. Wei et al., 2023) for E−113 and E−106 heat exchangers, which is considered at a cost coefficient of 0.354 $/GJ.

$$TAC = C \times \frac{1 \times [1+1]^s}{[1+1]^s - 1} + \text{energy cost} \tag{21}$$

By using Eq. (21) and the total amount of energy produced by the proposed system, the energy production cost has been calculated (Eq. (22)) (Mores et al., 2014). It is assumed that each working year is equal to 8150 h (H_y) (Abdelaziz et al., 2017).

$$\dot{C}_{energy}\left(\frac{\$}{kWh}\right) = \frac{TAC}{H_y \times \sum \text{energy product}} \tag{22}$$

In addition, Eq. (23) has been used to calculate the current net present value (NPV) index of the proposed structure. Eq. (24) has been used to calculate the ICF (income cash flow) parameter. A payback period of 3 years has been assumed (Xiao et al., 2023).

$$NPV = -D + \left[ICF \times \frac{(1+1)^s - 1}{1 \times (1+1)^s}\right] \tag{23}$$

$$ICF\left(\frac{\$}{year}\right) = \frac{D}{\text{payback period}} \tag{24}$$

The last parameter examined for the proposed process is the total unit cost of the product, which has been determined using Eq. (25) in this study (Cao et al., 2021). The symbol α represents the maintenance factor and its value is equal to 1.06.

Table 18
Results of equipment cost estimation.

Components	Z_i ($)	Components	Z_i ($)
ORC-octane	8588888	K-100	1291422
ORC-heptane	4605212	CRV-100	365845
ORC-pentane	3352646	E−112	238109
PEM electrolyser	22002385	E−101	2014869
E−104	399770	E−103	74362
E−105	33990	E−102	1036639
C-100 (Vessel)	542652	E−107	156049
P-100	679956	VLV-100	47310
S-100	81000	T-101	6359385
Z_{total} = 51870489 USD			

Table 19
Results of calculations for estimating the total capital investment cost.

Parameters	
Purchased-Equipment Cost	51870489
Purchased-Equipment installation	46683440
Piping	3630934
Instrumentation and Controls	20748196
Electrical Equipment and Materials	7780573
Land	5187049
Civil, Structural, and Architectural Work	46683440
Service Facilities	51870489
Total Direct Costs (A)	267133018
Engineering and Supervision	38902867
Construction Costs	40069953
Contingencies	20034976
Total Indirect Costs (B)	98709541
Total Fixed Capital Investment (C)	365842559
Startup Costs	44089916
Working Capital	97314121
Allowance for Funds Used During Construction	54876384
Total Capital Investment (D)	486570604

Table 20
Overall results for the economic assessment of the proposed process.

parameters	Value
Total Capital Investment ($)	486570604
Total Fixed Capital Investment ($)	365842559
Total Indirect Costs ($)	98709541
Total Direct Costs ($)	267133018
Total Annual Cost ($/year)	56652131
Cost of Energy $\left(\$/_{kWh}\right)$	0.0068
Cost of Electricity $\left(\$/_{kWh}\right)$	0.0313
Net Present Value ($)	587636274
Total Unit Cost of Product $\left(\$/_{GJ}\right)$	0.0274

$$C_{TUCP}\left(\frac{\$}{GJ}\right) = \frac{1 \times [1+1]^s}{[1+1]^s - 1} \times D \times \alpha \times \frac{1}{H_y \times \sum \text{exergy product}} \tag{25}$$

The cost of equipment is reported in Table 18. According to this table, the total equipment cost is $51,870,489. Based on this parameter, in Table 19, the total capital investment cost for the proposed structure is estimated to be $486,570,604. Other costs are also listed in Table 20. According to the estimates, the total annual cost of the polygeneration project is $56,652,131. Based on the total energy and generated power, the cost of each energy and power unit is 0.0068 $/kWh and 0.0313 $/kWh, respectively. The cost of energy (COE) is meager due to the heat integration and high production flow rate of products in the proposed process.

According to Table 21, the cost of produced electricity is significantly reduced compared to other articles. This indicates that generating power as a product from the proposed process (Fig. 3) would be more

Table 21
Comparing the cost of electricity parameter with other papers.

Studies	Process	COE($\$/_{kWh}$)	Reduction (%)
Ref (Rokhmawati et al., 2023)	Coal-fired power plant generation	0.05	37.4
Ref (Mores et al., 2014)	Standalone NGCC	0.0541	42.14
Ref (Mores et al., 2014)	NGCC + CO_2 capture	0.0807	61.21
Ref (Fisher et al., 2005)	NGCC + CO_2 capture	0.0632	50.47
Ref (Abu-Zahra et al., 2007)	CO_2 capture from power plants	0.056	44.11
Ref (Shen et al., 2020)	Biomass power plant	0.194–0.351	83.87–91.08
Current study	Polygeneration system based on Tars	0.0313	–

Table 22
The amount of total annual cost savings ($\dot{C}^{TAC}_{saving}$) compared to other power generation methods.

Process	ΔCOE($\$/_{kWh}$)	$\dot{C}^{TAC}_{saving}$ ($ /year)
Standalone NGCC (Mores et al., 2014)	0.0228	41270622
NGCC + CO_2 capture (Mores et al., 2014)	0.0557	100823406
NGCC + CO_2 capture (Fisher et al., 2005)	0.0319	57742669
CO_2 capture from power plants (Abu-Zahra et al., 2007)	0.0247	44709841
Coal-fired power plant generation (Rokhmawati et al., 2023)	0.0187	33849151

economically feasible compared to an NGCC power plant. As Table 22 shows, if electricity is produced through the proposed system, $41,270,622 will be saved annually in factory costs. This amount has been estimated to be $33,849,151 per year compared to a coal-fired power generation system (Table 22). The results also indicate that using the proposed structure has a positive economic value (NPV) of $587,636,274. Finally, it is determined that the cost of producing each unit of exergy through the proposed system is equal to $0.0274. This shows that the presented process can produce practical work at the lowest possible cost.

In addition, according to Eq. (26), the amount of savings in annual costs for power generation compared to previous works (Fisher et al., 2005; Mores et al., 2014; Rokhmawati et al., 2023; Shen et al., 2020) and examined systems for power generation have also been calculated and reported in Table 22.

$$\dot{C}^{TAC}_{saving}\left(\frac{\$}{year}\right) = \Delta COE \times \dot{W}^{proposed}_{net} \times H_y \tag{26}$$

$$\Delta COE\left(\frac{\$}{kWh}\right) = COE_{Ref} - COE_{proposed} \tag{27}$$

Table 23
Considered parametric for parametric study.

Parameter	Range	Base design condition
Exiting flue gas temperature	From 30 to 80 °C	50 °C
Fuel flow rate of the electrolyzer	From 1000 to 3700 kmol/h	1000 kmol/h
Inlet hot stream ratio to ORC-C_7	From 0 to 1	0.50
Inlet hot stream ratio to the GUS subsystem	From 0.3 to 0.95	0.28

5. Results and discussions

This section presents the outcomes of the parametric analysis conducted using the simulation. Based on this objective, a set of four distinct parameters are carefully chosen and their impact on the key performance indicators is investigated. Table 23 presents the parameters that are considered, along with their selected range and the base design condition.

The temperature of the flue gas exiting the E−112 heat exchanger (T^{flue}_{out}) is a crucial parameter in the presented process, which affects thermodynamic, environmental, and economic indicators. According to Fig. 10, increasing this temperature decreases the total exergy level associated with the products, CHP efficiency, and exergy efficiency. Based on various simulation tests, the main reason for this downward trend is the decrease in exergy level of produced electricity and increased irreversibility in the entire process. Therefore, it is better to have a higher value of T^{flue}_{out} for increasing the production rate of products and system efficiency. Based on the findings in Fig. 11, it can be concluded that there is a negative correlation between T^{flue}_{out} and the total energy output. As a result, the COE parameter experiences an increase. According to Eq. (22), the COE index is inverse to the overall energy generated from the process. Therefore, reducing the energy product will also increase its production cost. Additionally, increasing the T^{flue}_{out} parameter increases pollution intensity (SCE). Each unit of exergy will also be produced at a higher cost, which is undesirable. The decrease in the exergy product value explains the reason for the increasing trend of TUCP in Fig. 10.

In Figs. 12 and 13, the second parameter affecting the entire proposed system, which is the fuel flow rate of the PEM electrolyzer (F^{PEM}_{water}), has been investigated. Fig. 12 shows that as the value of F^{PEM}_{water} increases, all four thermodynamic efficiencies show a downward trend. According to Fig. 13, the main reason for this decrease in thermodynamic performance is the reduction in energy product, exergy product, and net power product values. As the parameter F^{PEM}_{water} increases, the power consumption of the electrolyzer increases. This phenomenon results in a decrease in the overall net power and, consequently, a reduction in the overall electrical efficiency, according to Eq. (11). The decrease in net power in the entire process reduces the exergy product and energy product. As a result, the efficiency of CHP, energy efficiency, and exergy efficiency are affected, and their trend, according to Fig. 12, is decreasing.

Fig. 14 shows that with an increase in the F^{PEM}_{water} parameter, the TUCP index follows an upward trend. This is because the trend in exergy production, resulting from net power generation, is also reduced. Furthermore, the SCE index decreases, indicating an inverse relation

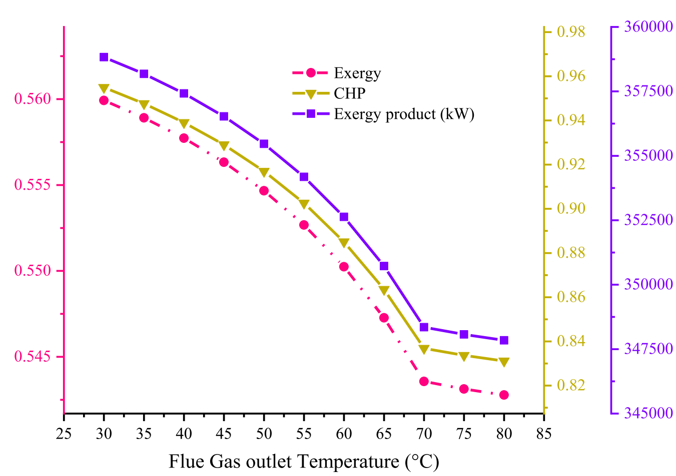

Fig. 10. Investigating the effect of changes in the exiting flue gas temperature on overall exergy efficiency, CHP efficiency, and exergy production.

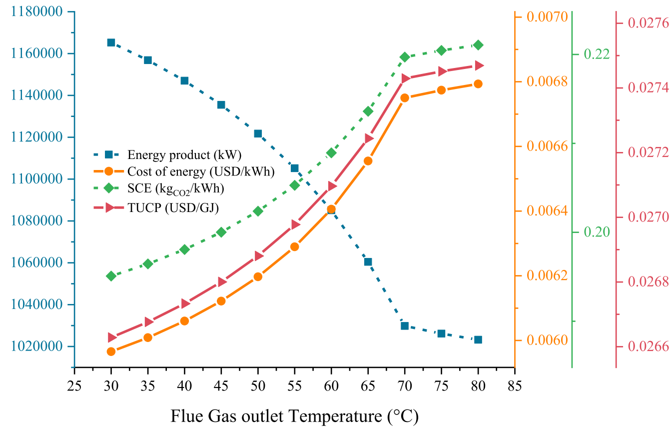

Fig. 11. Investigating the effect of changes in the exiting flue gas temperature on SCE environmental index and the TUCP thermoeconomic index and overall energy production and its production cost.

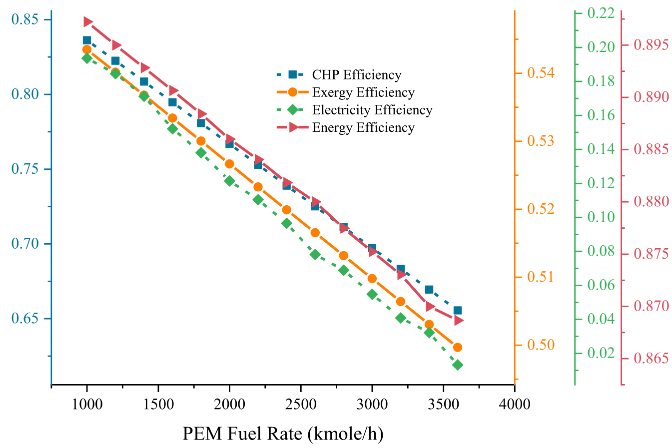

Fig. 12. Investigating the effect of changes in the fuel flow rate of the electrolyzer on thermodynamic efficiencies.

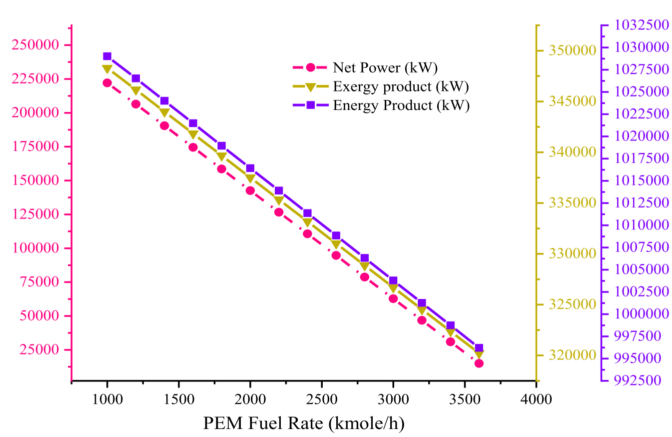

Fig. 13. Investigating the effect of changes in the fuel flow rate of the electrolyzer on energy production, exergy production, and net power product.

between F_{water}^{PEM} and pollution intensity in the entire process.

The third important and effective parameter in the proposed process is the flow ratio of the branched hot stream to the organic Rankine cycle with heptane working fluid (α_{ORC-C7}^{FR}). According to Fig. 15, when the α_{ORC-C7}^{FR} parameter increases (more hot fluid is directed towards ORC-C_7), it leads to an increase in net power generation, exergy efficiency,

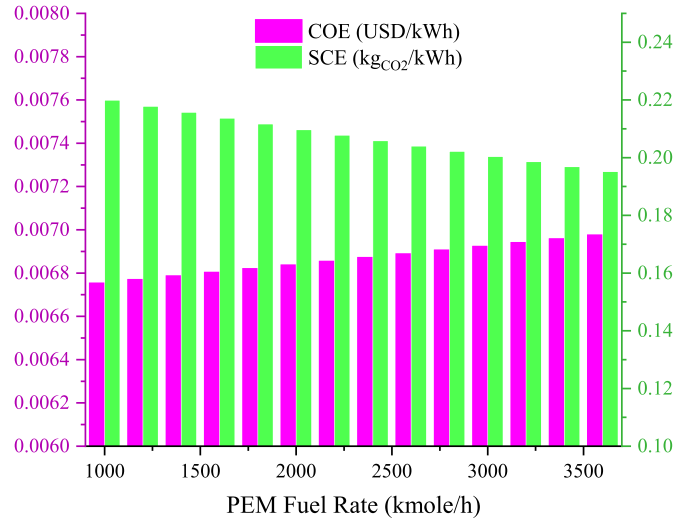

Fig. 14. Investigating the effect of changes in the fuel flow rate of the electrolyzer on the SCE environmental index and the COE thermoeconomic index.

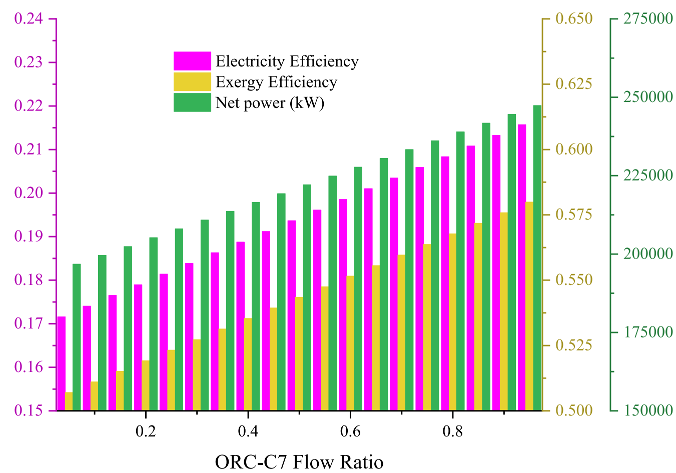

Fig. 15. Investigating the inlet hot stream ratio to ORC-C_7 on thermodynamic efficiencies and net power generation.

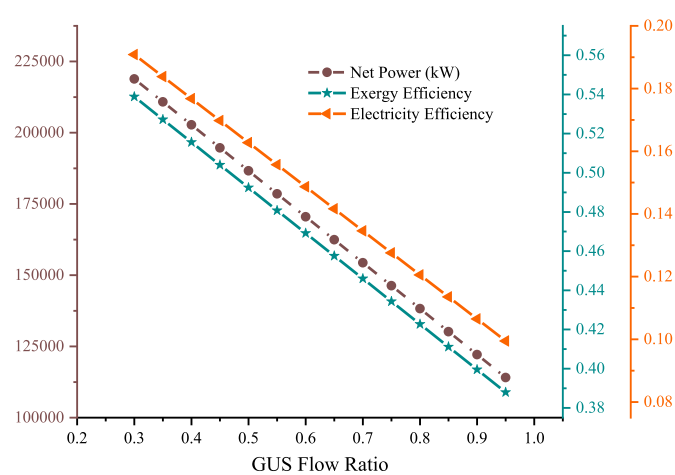

Fig. 16. Investigating the inlet hot stream ratio to the GUS subsystem on electrical efficiency, exergy efficiency, and net power generation.

and electrical efficiency in the entire system. The reason for this is the higher exergy efficiency of the ORC-C_7 cycle compared to ORC-C_5 as shown in Fig. 16.

The third essential and effective parameter in the proposed process is the flow ratio of the branched hot stream to the ORC with heptane working fluid (α^{FR}_{ORC-C7}). According to Fig. 15, when the α^{FR}_{ORC-C7} parameter increases (more hot fluid is directed toward ORC-C7). This change increases net power generation, exergy efficiency, and electrical efficiency in the entire system. The reason for this is the higher exergy efficiency of the ORC-C7 cycle compared to ORC-C5, as shown in Fig. 16. Therefore, increasing the α^{FR}_{ORC-C7} parameter generates more net power, which ultimately leads to an increase in electrical efficiency. The fourth important parameter, whose effects are evaluated in Fig. 16, is the flow ratio of the branched hot stream to the GUS subsystem (α^{FR}_{GUS}). According to Fig. 16, increasing the α^{FR}_{GUS} parameter decreases the thermodynamic performance of the system and reduces net power generation. The main reason for this is, based on Fig. 16, the lower exergy efficiency of the GUS subsystem compared to the LGTS section. Therefore, sending more hot streams as a heat source towards the GUS section causes a decrease in electrical and exergy efficiencies due to the reduction in net power output.

Based on the conducted simulation, detailed information regarding the operational parameters of the components and their corresponding states can be found in Tables 24–26. The data obtained for the components is presented in Table 24. The operational conditions pertaining to pressure, temperature, and molar flow rate for all states involved in the proposed process are presented in Table 25. Furthermore, the composition of the stream at the main states is presented in Table 26.

Table 24
Specifications and conditions governing the equipment used in the process.

Pumps					
Component	η_p (%)	$\dot{W}$ (kW)	P_{in} (kPa)	$\dot{m}_{in}$ (kg/s)	P_{out} (kPa)
P-100	85	1645	150	500	2050
P-101	85	1055	7.847	537.1	1000
P-102	85	999.1	109.9	735.4	736.9
P-103	85	4418	28.09	1090	2000
P-104	85	44.05	113	6.637	5000
Heat Exchangers					
Component	LMTD (°C)	Heat duty (kW)	Min. approach (°C)	Hot Pinch Temp (°C)	Cold Pinch Temp (°C)
E−100	218.8	1197000	4.1	90	85.9
E−112	44.62	11650	40	90	50
E−108	76.51	362400	54.86	84.95	30.09
E−109	27.91	290300	9.65	29.65	20
E−110	115.2	362400	54.43	84.95	30.53
E−111	12.58	318300	10.19	30.19	20
E−101	7.79	216200	3.45	12.13	8.65
E−103	18	12530	0.82	106.82	106
E−104	14.06	3708	9.13	118.13	109
E−105	5.41	289400	2.15	5	2.85
E−107	61.41	116600	62.3	112.3	50
Turbine					
Component	η_T (%)	$\dot{W}$ (kW)	P_{in} (kPa)	$\dot{m}_{in}$ (kg/s)	P_{out} (kPa)
T-100	85	194500	2000	1090	28.09
T-101	85	20980	2050	85.39	150
T-102	85	73160	1000	537.1	7.847
T-103	85	45010	736.9	735.4	109.9
Columns					
Component	High (m)	ΔP(kPa)	Diameter (m)	Number of stages	Reflux Ratio
C-101	4.5	0	1.56	1	0
Compressors					
Component	η_C (%)	$\dot{W}$ (kW)	P_{in} (kPa)	$\dot{m}_{in}$ (kg/s)	P_{out} (kPa)
K-100	85	236300	101.3	330	200
Interstage Coolers					
Component	T_{in} (°C)	T_{out} (°C)	ΔP(kPa)	$\dot{W}$(kW)	$\dot{m}_{in}$ (kg/s)
E−106	21.17	8.364	0.0	136200	500
E−113	80.1	70.1	47	70.94	1.633
Separators					
Component	T_{in} (°C)	T_{out} (°C)	ΔP(kPa)	$\dot{m}_l$ (kg/s)	$\dot{m}_v$ (kg/s)
S-100	91.44	91.44	0.0	12.39	85.39

6. Conclusion

The use of tar produced from biomass processing had yet to be previously integrated into biomass-based energy applications. Therefore, the current study investigated the practicability of using tar as the primary fuel source in an innovative energy system. By employing an innovative thermal integration approach, this process effectively generated multiple forms of energy and energy-based products, namely electricity, hot water, chilled water, oxygen, and hydrogen. The system configuration was simulated using the Aspen HYSYS software, wherein a comprehensive assessment encompassing energy, exergy, economic, and environmental factors was conducted. Moreover, a sensitivity analysis was carried out to explore the impact of operational parameters on the crucial variables. The main outcomes derived from this study are as follows:

- The baseline simulation mode of the system demonstrates its ability to generate 7920.65 kg/s of hot water at a temperature of 50 °C, as well as 33.52 kg/s of cold water at 5 °C. Furthermore, it can produce 0.56 kg/s of hydrogen product and 4.444 kg/s of oxygen product through a PEM electrolyzer. Additionally, the system can generate a considerable power output of 222100 kW.
- The findings demonstrate that the process under consideration exhibits total energy and exergy efficiencies of 89.72% and 54.35%, respectively.
- From the viewpoint of the first and second laws of thermodynamics, the section of the proposed process that exhibited the least efficiency is the tars fuel combustion, as it solely generated hot water as its output through the E−112 heat exchanger.
- Based on the environmental assessment findings, it has been determined that the new structure exhibited zero indirect CO_2 emission. This outcome can be attributed to the system's comprehensive utilization of thermal integration. In contrast, it is observed that the CO_2 emission intensity was 0.22 kg/kWh, demonstrating a noteworthy reduction in comparison to analogous procedures.
- Based on economic evaluation, the cost of energy, electricity, and TUCP were equal to 0.0068 $/kWh, 0.0313 $/kWh, and 0.0274 $/GJ, respectively. Moreover, determining the net present value yields a significant amount of $587,636,274.
- The conducted parametric study revealed a direct correlation between the augmentation of the flow ratio toward ORC-C7 and the corresponding rise in both exergy efficiency and net power generation. The aforementioned difference can be attributed to the superior exergy efficiency exhibited by ORC-C7 in comparison to ORC-C5.
- The primary determinant in reducing net power generation and overall exergy efficiency was found to be the augmentation of the fuel flow rate of the PEM electrolyzer.
- The GUS subsystem showed a lower exergy efficiency when compared to the LGTS subsystem. Therefore, it is recommended to direct a higher flow rate of hot fluid toward the LGTS subsystem for

Table 25
The operational conditions for all states of the proposed process.

Stream	T (^{o}C)	P (kPa)	F (kmole/h)	stream	T (^{o}C)	P (kPa)	F(kmole/h)
1	700	200	29420	2	25	101.3	41180
3	95.43	200	41180	4	374.6	200	70590
5	1794	200	65840	7	90	200	65840
8	85.9	2000	34360	9	400	2000	34340
10	329.1	28.09	34340	11	329.1	28.09	9615
12	329.1	28.09	24720	13	8.366	150	102400
14	8.685	2050	102400	15	8.685	2050	5122
16	8.685	2050	97320	17	103.2	2050	97320
18	103.1	2050	105000	19	106.8	2050	20580
20	125	2050	84410	21	118.1	28.09	9615
22	91.44	2050	20580	23	106	2050	5122
24	91.44	2050	18030	25	91.44	2050	2548
26	91.44	2050	2548	27	106	2050	5122
28	109	2050	18030	29	112.3	28.09	9615
30	2.847	150	18030	31	25	100	6699
32	5	100	6699	33	12	150	18030
34	12.13	2050	84410	35	12.56	150	84410
36	21.17	150	102400	37	8.364	150	102400
38	84.96	28.09	9615	39	20	200	180000
40	50	200	180000	41	329.1	28.09	12360
42	329.1	28.09	12360	43	84.96	28.09	12360
44	30.09	1000	19300	45	200.9	1000	19300
46	126.7	7.847	19300	47	29.65	7.847	19300
48	20	200	140900	49	50	200	140900
50	30.09	1000	19300	51	84.96	28.09	12360
52	30.53	736.9	36700	53	109.9	736.9	36700
54	69.30	109.9	36700	55	30.19	109.9	36700
56	20	200	491400	57	50	200	491400
58	30.57	736.9	36700	59	84.96	28.09	34340
60	85.90	2000	34340	61	70.11	200	65840
62	20	200	17980	63	50	200	17980
66	54.10	113	1000	67	58.27	113	1326
68	79.90	5000	1517	69	79.90	5000	308.9
70	58.78	5000	1326	71	80	4900	1000
72	80.10	4850	826.3	73	80.1	4850	500
74	80.10	4706	326.3	75	70.1	4659	326.3
76	70.1	4659	326.3				

Table 26
Stream's composition for main states.

Components	1	2	14	61	71	73	68
	Mass Fraction						
H_2O	0.0604	0.0000	0.5623	0.0987	0.0000	0.0000	0.0172
O_2	0.0000	0.2329	0.0000	0.0159	0.0000	1	0.8728
H_2	0.0151	0.0000	0.0000	0.0000	1	0.0000	0.1100
CH_4	0.0276	0.0000	0.0000	0.0000	0.0000	0.0000	0.0000
N_2	0.4525	0.7671	0.0000	0.6484	0.0000	0.0000	0.0000
Benzene	0.0064	0.0000	0.0000	0.0000	0.0000	0.0000	0.0000
Octane	0.0000	0.0000	0.0000	0.0000	0.0000	0.0000	0.0000
CO	0.1627	0.0000	0.0000	0.0000	0.0000	0.0000	0.0000
CO_2	0.2754	0.0000	0.0000	0.2370	0.0000	0.0000	0.0000
NH_3	0.0000	0.0000	0.4377	0.0000	0.0000	0.0000	0.0000

optimal performance. This measure acted as a preventative strategy against the decline in electricity generation and thermodynamic efficiency while mitigating CO_2 emissions.

CRediT authorship contribution statement

Mohamad Abou Houran: Resources, Formal analysis, Investigation, Supervision, Methodology, Writing - original draft. **Mohamed A. Habila:** Methodology, Writing – original draft, Investigation, Resources. **Fahid Riaz:** Writing – review & editing, Methodology, Formal analysis, Data curation. **Manoj Kumar Agrawal:** Methodology, Writing – original draft, Data curation, Resources. **Kwanho Shi:** Writing – review & editing, Supervision, Resources.

Declaration of competing interest

The authors declare that they have no known competing financial interests or personal relationships that could have appeared to influence the work reported in this paper.

Data availability

Data will be made available on request.

Acknowledgments

- This work was funded by the National Natural Science Foundation of China (Grant Number 52150410418)
- This work was funded by the Researchers Supporting Project

Number (RSP2023R441), King Saud University, Riyadh, Saudi Arabia.
- Authors acknowledge financial support from Abu Dhabi University's Office of Research and Sponsored Programs.

References

Abdelaziz, O.Y., Hosny, W.M., Gadalla, M.A., Ashour, F.H., Ashour, I.A., Hulteberg, C.P., 2017. Novel process technologies for conversion of carbon dioxide from industrial flue gas streams into methanol. J. CO2 Util. 21, 52–63.
Abu-Zahra, M.R.M., Niederer, J.P.M., Feron, P.H.M., Versteeg, G.F., 2007. CO2 capture from power plants: Part II. A parametric study of the economic performance based on mono-ethanolamine. Int. J. Greenh. Gas Control 1 (2), 135–142.
Ahmadi, P., Dincer, I., Rosen, M.A., 2013. Development and assessment of an integrated biomass-based multi-generation energy system. Energy 56, 155–166.
Ahmadi, P., Rosen, M.A., Dincer, I., 2011. Greenhouse gas emission and exergo-environmental analyses of a trigeneration energy system. Int. J. Greenh. Gas Control 5 (6), 1540–1549.
Ahmadi, S., Ghaebi, H., Shokri, A., 2019. A comprehensive thermodynamic analysis of a novel CHP system based on SOFC and APC cycles. Energy 186, 115899.
Akrami, E., Khazaee, I., Gholami, A., 2018. Comprehensive analysis of a multi-generation energy system by using an energy-exergy methodology for hot water, cooling, power and hydrogen production. Appl. Therm. Eng. 129, 995–1001.
Anis, S., Zainal, Z.A., 2011. Tar reduction in biomass producer gas via mechanical, catalytic and thermal methods: a review. Renew. Sustain. Energy Rev. 15 (5), 2355–2377.
Ansari, S.A., Kazim, M., Khaliq, M.A., Ratlamwala, T.A.H., 2021. Thermal analysis of multigeneration system using geothermal energy as its main power source. Int. J. Hydrogen Energy 46 (6), 4724–4738.
Anvari, S., Khalilarya, S., Zare, V., 2019. Power generation enhancement in a biomass-based combined cycle using solar energy: thermodynamic and environmental analysis. Appl. Therm. Eng. 153, 128–141.
Asgari, N., Saray, R.K., Mirmasoumi, S., 2020. Energy and exergy analyses of a novel seasonal CCHP system driven by a gas turbine integrated with a biomass gasification unit and a LiBr-water absorption chiller. Energy Convers. Manag. 220, 113096.
Auñón-Hidalgo, J.A., Sidrach-de-Cardona, M., Auñón-Rodríguez, F., 2021. Performance and CO2 emissions assessment of a novel combined solar photovoltaic and thermal, with a Stirling engine micro-CHP system for domestic environments. Energy Convers. Manag. 230, 113793.
Azariyan, H., Vajdi, M., Takleh, H.R., 2021. Assessment of a high-performance geothermal-based multigeneration system for production of power, cooling, and hydrogen: thermodynamic and exergoeconomic evaluation. Energy Convers. Manag. 236, 113970.
Baak, J.A., Pozarlik, A.K., Arentsen, M.J., Brem, G., 2019. Techno-economic study of a zero-emission methanol-based energy storage system. Energy Convers. Manag. 182, 530–545.
Bellos, E., Tzivanidis, C., 2018. Multi-objective optimization of a solar driven trigeneration system. Energy 149, 47–62.
Bellotti, D., Rivarolo, M., Magistri, L., Massardo, A.F., 2017. Feasibility study of methanol production plant from hydrogen and captured carbon dioxide. J. CO2 Util. 21, 132–138.
Bhaduri, S., Contino, F., Jeanmart, H., Breuer, E., 2015. The effects of biomass syngas composition, moisture, tar loading and operating conditions on the combustion of a tar-tolerant HCCI (Homogeneous Charge Compression Ignition) engine. Energy 87, 289–302.
Briones-Hidrovo, A., Copa, J., Tarelho, L.A.C., Gonçalves, C., da Costa, T.P., Dias, A.C., 2021. Environmental and energy performance of residual forest biomass for electricity generation: gasification vs. combustion. J. Clean. Prod. 289, 125680.
Cao, Y., Dhahad, H.A., Farouk, N., Xia, W.-F., Rad, H.N., Ghasemi, A., Kamranfar, S., Sani, M.M., Shayesteh, A.A., 2021a. Multi-objective bat optimization for a biomass gasifier integrated energy system based on 4E analyses. Appl. Therm. Eng. 196, 117339.
Cao, Y., Dhahad, H.A., Parikhani, T., Anqi, A.E., Mohamed, A.M., 2021b. Thermo-economic evaluation of a combined Kalina cycle and humidification-dehumidification (HDH) desalination system integrated with thermoelectric generator and solar pond. Int. J. Heat Mass Tran. 168, 120844.
Cao, Y., Haghghi, M.A., Shamsaiee, M., Athari, H., Ghaemi, M., Rosen, M.A., 2020. Evaluation and optimization of a novel geothermal-driven hydrogen production system using an electrolyser fed by a two-stage organic Rankine cycle with different working fluids. J. Energy Storage 32, 101766.
Cardoso, J., Silva, V., Eusebio, D., 2019. Techno-economic analysis of a biomass gasification power plant dealing with forestry residues blends for electricity production in Portugal. J. Clean. Prod. 212, 741–753.
Chen, H., Alzahrani, H.A., Amin, M.A., Sun, M., 2023. Towards sustainable development through the design, multi-aspect analyses, and multi-objective optimization of a novel solar-based multi-generation system. Energy 267, 126507.
Chen, Y., Feng, L., Jamal, S.S., Sharma, K., Mahariq, I., Jarad, F., Arsalanloo, A., 2021. Compound usage of L shaped fin and Nano-particles for the acceleration of the solidification process inside a vertical enclosure (A comparison with ordinary double rectangular fin). Case Stud. Therm. Eng. 28, 101415.
Chitsaz, A., Haghghi, M.A., Hosseinpour, J., 2019. Thermodynamic and exergoeconomic analyses of a proton exchange membrane fuel cell (PEMFC) system and the feasibility evaluation of integrating with a proton exchange membrane electrolyzer (PEME). Energy Convers. Manag. 186, 487–499.
Dincer, I., Rosen, M.A., 2012. Exergy: Energy, Environment and Sustainable Development. Newnes.
Ehyaei, M.A., Rosen, M.A., 2019. Optimization of a triple cycle based on a solid oxide fuel cell and gas and steam cycles with a multiobjective genetic algorithm and energy, exergy and economic analyses. Energy Convers. Manag. 180, 689–708.
Ersöz, A., DurakÇetin, Y., Sarıoğlan, A., Turan, A.Z., Mert, M.S., Yüksel, F., Figen, H.E., Güldal, N.Ö., Karaismailoğlu, M., Baykara, S.Z., 2018. Investigation of a novel & integrated simulation model for hydrogen production from lignocellulosic biomass. Int. J. Hydrogen Energy 43 (2), 1081–1093.
Fan, G., Ahmadi, A., Ehyaei, M.A., Das, B., 2021. Energy, exergy, economic and exergoenvironmental analyses of polygeneration system integrated gas cycle, absorption chiller, and Copper-Chlorine thermochemical cycle to produce power, cooling, and hydrogen. Energy 222, 120008.
Fan, J., Hong, H., Zhu, L., Wang, Z., Jin, H., 2017. Thermodynamic evaluation of chemical looping combustion for combined cooling heating and power production driven by coal. Energy Convers. Manag. 135, 200–211.
Fisher, K.S., Beitler, C., Rueter, C., Searcy, K., Rochelle, G., Jassim, M., 2005. Integrating MEA Regeneration with CO2 Compression and Peaking to Reduce CO2 Capture Costs. Trimeric Corporation.
Ghorbani, S., Khoshgoftar-Manesh, M.H., Nourpour, M., Blanco-Marigorta, A.M., 2020. Exergoeconomic and exergoenvironmental analyses of an integrated SOFC-GT-ORC hybrid system. Energy 206, 118151.
Ghorbannejad, F., Manesh, M.H.K., Nemati, M., Ghasemi, A., 2022. A comprehensive exergoenvironment-emergoeconomic-emergoenvironment based analysis of hybrid steam biomass gasification and solid oxide fuel cell system for a multigeneration system. Energy Rep. 8, 9057–9080.
Gu, H., Liu, J., Zhou, X., Wu, Q., Liu, Y., Yu, S., Qiu, W., Xu, J., 2023. Modelling of a novel electricity and methanol co-generation using heat recovery and CO2 capture: comprehensive thermodynamic, economic, and environmental analyses. Energy 278, 127481.
Guedri, K., Singh, P., Riaz, F., Inayat, A., Shah, N.A., Fadhl, B.M., Makhdoum, B.M., Arsalanloo, A., 2023. Solidification acceleration of phase change material in a horizontal latent heat thermal energy storage system by using spiral fins. Case Stud. Therm. Eng. 48, 103157.
Guo, Y., Yu, Z., Li, G., Zhao, H., 2020. Performance assessment and optimization of an integrated solid oxide fuel cell-gas turbine cogeneration system. Int. J. Hydrogen Energy 45 (35), 17702–17716.
Haghghi, M.A., Holagh, S.G., Chitsaz, A., Parham, K., 2019. Thermodynamic assessment of a novel multi-generation solid oxide fuel cell-based system for production of electrical power, cooling, fresh water, and hydrogen. Energy Convers. Manag. 197, 111895.
Haghghi, M.A., Mohammadi, Z., Delpisheh, M., Nadimi, E., Athari, H., 2023. Multi-variable study/optimization of a novel geothermal-driven poly-generation system: application of a soft-computing intelligent procedure and MOGWO. Process Saf. Environ. Protect. 171, 507–531.
Hamedani, S.R., Villarini, M., Marcantonio, V., di Matteo, U., Monarca, D., Colantoni, A., 2023. Comparative energy and environmental analysis of different small-scale biomass-fueled CCHP systems. Energy 263, 125846.
Islam, S., Dincer, I., Yilbas, B.S., 2018. Development, analysis and assessment of solar energy-based multigeneration system with thermoelectric generator. Energy Convers. Manag. 156, 746–756.
Jana, K., De, S., 2015. Polygeneration using agricultural waste: thermodynamic and economic feasibility study. Renew. Energy 74, 648–660.
Javadi, M.A., Abhari, M.K., Ghasemiasl, R., Ghomashi, H., 2021. Energy, exergy and exergy-economic analysis of a new multigeneration system based on double-flash geothermal power plant and solar power tower. Sustain. Energy Technol. Assessments 47, 101536.
Jia, J., Zang, G., Paul, M.C., 2021. Energy, exergy, and economic (3E) evaluation of a CCHP system with biomass gasifier, solid oxide fuel cells, micro-gas turbine, and absorption chiller. Int. J. Energy Res. 45 (10), 15182–15199.
Jiang, P., Bai, H., Xu, Q., Arsalanloo, A., 2023. Thermodynamic, exergoeconomic, and economic analyses with multi-objective optimization of a novel liquid air energy storage coupled with an off-shore wind farm. Sustain. Cities Soc. 90, 104353.
Ji-chao, Y., Sobhani, B., 2021. Integration of biomass gasification with a supercritical CO2 and Kalina cycles in a combined heating and power system: a thermodynamic and exergoeconomic analysis. Energy 222, 119980.
Khalid, F., Dincer, I., Rosen, M.A., 2016. Techno-economic assessment of a renewable energy based integrated multigeneration system for green buildings. Appl. Therm. Eng. 99, 1286–1294.
Kianfard, H., Khalilarya, S., Jafarmadar, S., 2018. Exergy and exergoeconomic evaluation of hydrogen and distilled water production via combination of PEM electrolyzer, RO desalination unit and geothermal driven dual fluid ORC. Energy Convers. Manag. 177, 339–349.
Li, H.-M., Li, G.-X., Li, L., 2023. Comparative investigation on combustion characteristics of ADN-based liquid propellants in inert gas and oxidizing gas atmospheres with resistive ignition method. Fuel 334, 126742.
Li, J., Tao, J., Yan, B., Jiao, L., Chen, G., Hu, J., 2021. Review of microwave-based treatments of biomass gasification tar. Renew. Sustain. Energy Rev. 150, 111510.
Li, Y., Zhang, G., Yang, Y., Zhai, D., Zhang, K., Xu, G., 2014. Thermodynamic analysis of a coal-based polygeneration system with partial gasification. Energy 72, 201–214.
Liao, G., Jiaqiang, E., Zhang, F., Chen, J., Leng, E., 2020. Advanced exergy analysis for Organic Rankine Cycle-based layout to recover waste heat of flue gas. Appl. Energy 266, 114891.
Lin, H., Wu, X., Ayed, H., Mouldi, A., Abbas, S.Z., Ebrahimi-Moghadam, A., 2022. A new biomass gasification driven hybrid system for power and liquid hydrogen

cogeneration: parametric study and multi-objective evolutionary optimization. Int. J. Hydrogen Energy 47 (62), 26394–26407.
Liu, L., Tang, Y., Liu, D., 2022. Investigation of future low-carbon and zero-carbon fuels for marine engines from the view of thermal efficiency. Energy Rep. 8, 6150–6160.
Liu, X., Zhao, H., Huang, Z., Shi, S., Guo, R., Ding, P., Xie, S., 2023a. A comprehensive study of a novel multigeneration system using a combined power plant based on geothermal energy and oxyfuel combustion. J. Clean. Prod. 408, 137098.
Liu, X., Zhao, H., Huang, Z., Shi, S., Guo, R., Ding, P., Xie, S., 2023b. A comprehensive study of a novel multigeneration system using a combined power plant based on geothermal energy and oxyfuel combustion. J. Clean. Prod. 408, 137098.
Lopez-Echeverry, J.S., Reif-Acherman, S., Araujo-Lopez, E., 2017. Peng-Robinson equation of state: 40 years through cubics. Fluid Phase Equil. 447, 39–71.
Lv, S., Zhang, B., Ji, Y., Ren, J., Yang, J., Lai, Y., Chang, Z., 2023. Comprehensive research on a high performance solar and radiative cooling driving thermoelectric generator system with concentration for passive power generation. Energy 275, 127390.
Mansouri, R., Boukholda, I., Bourouis, M., Bellagi, A., 2015. Modelling and testing the performance of a commercial ammonia/water absorption chiller using Aspen-Plus platform. Energy 93, 2374–2383.
Miao, Z., Meng, X., Zhou, S., Zhu, M., 2020. Investigation for power generation based on single-vertex movement of thermoelectric module. Sustain. Cities Soc. 53, 101929.
Mohammadi, K., Khanmohammadi, S., Khorasanizadeh, H., Powell, K., 2020. A comprehensive review of solar only and hybrid solar driven multigeneration systems: classifications, benefits, design and prospective. Appl. Energy 268, 114940.
Moran, M.J., Tsatsaronis, G., 2017. Engineering thermodynamics. In: CRC Handbook of Thermal Engineering. CRC Press, pp. 1–112.
Mores, P.L., Godoy, E., Mussati, S.F., Scenna, N.J., 2014. A NGCC power plant with a CO2 post-combustion capture option. Optimal economics for different generation/capture goals. Chem. Eng. Res. Des. 92 (7), 1329–1353.
MosayebNezhad, M., Mehr, A.S., Lanzini, A., Misul, D., Santarelli, M., 2019. Technology review and thermodynamic performance study of a biogas-fed micro humid air turbine. Renew. Energy 140, 407–418.
Petrecca, G., 2014. Energy Conversion and Management. Springer International Publishing, Cham.
Rahimpour, M.R., Jamshidnejad, Z., Jokar, S.M., Karimi, G., Ghorbani, A., Mohammadi, A.H., 2012. A comparative study of three different methods for flare gas recovery of Asalooye Gas Refinery. J. Nat. Gas Sci. Eng. 4, 17–28.
Ramesh, G.K., Madhukesh, J.K., Shah, N.A., Yook, S.-J., 2023. Flow of hybrid CNTs past a rotating sphere subjected to thermal radiation and thermophoretic particle deposition. Alex. Eng. J. 64, 969–979.
Razeghi, G., Zhang, L., Brown, T., Samuelsen, S., 2014. Impacts of plug-in hybrid electric vehicles on a residential transformer using stochastic and empirical analysis. J. Power Sources 252, 277–285.
Razmi, A.R., Afshar, H.H., Pourahmadiyan, A., Torabi, M., 2021. Investigation of a combined heat and power (CHP) system based on biomass and compressed air energy storage (CAES). Sustain. Energy Technol. Assessments 46, 101253.
Ren, J., Cao, J.-P., Yang, F.-L., Liu, Y.-L., Tang, W., Zhao, X.-Y., 2021. Understandings of catalyst deactivation and regeneration during biomass tar reforming: a crucial review. ACS Sustain. Chem. Eng. 9 (51), 17186–17206.
Rian, A.B., Ertesvåg, I.S., 2012. Exergy evaluation of the arctic snøhvit liquefied natural gas processing plant in northern Norway–significance of ambient temperature. Energy Fuel. 26 (2), 1259–1267.
Rokhmawati, A., Sugiyono, A., Efni, Y., Wasnury, R., 2023. Quantifying social costs of coal-fired power plant generation. Geograph. Sustain. 4 (1), 39–48.
Roy, D., Samanta, S., Ghosh, S., 2019. Techno-economic and environmental analyses of a biomass-based system employing solid oxide fuel cell, externally fired gas turbine and organic Rankine cycle. J. Clean. Prod. 225, 36–57.
Sadat, S.M.S., Ghaebi, H., Lavasani, A.M., 2020. 4E analyses of an innovative polygeneration system based on SOFC. Renew. Energy 156, 986–1007.
Shen, W., Chen, X., Qiu, J., Hayward, J.A., Sayeef, S., Osman, P., Meng, K., Dong, Z.Y., 2020. A comprehensive review of variable renewable energy levelized cost of electricity. Renew. Sustain. Energy Rev. 133, 110301.
Siddiqui, O., Ishaq, H., Dincer, I., 2019. A novel solar and geothermal-based trigeneration system for electricity generation, hydrogen production and cooling. Energy Convers. Manag. 198, 111812.
Suleman, F., Dincer, I., Agelin-Chaab, M., 2014. Development of an integrated renewable energy system for multigeneration. Energy 78, 196–204.
Sun, Z., Wang, T., Zhang, R., Li, H., Wu, Y., Toan, S., Sun, Z., 2023. Boosting hydrogen production via deoxygenation-sorption-enhanced biomass gasification. Bioresour. Technol. 382, 129197.
Tabriz, Z.H., Khani, L., Mohammadpourfard, M., Akkurt, G.G., 2022. Biomass Driven Polygeneration Systems: A Review of Recent Progress and Future Prospects. Process Safety and Environmental Protection.
Udeh, G.T., Michailos, S., Ingham, D., Hughes, K.J., Ma, L., Pourkashanian, M., 2021. A techno-enviro-economic assessment of a biomass fuelled micro-CCHP driven by a hybrid Stirling and ORC engine. Energy Convers. Manag. 227, 113601.
Vidal, A., Best, R., Rivero, R., Cervantes, J., 2006. Analysis of a combined power and refrigeration cycle by the exergy method. Energy 31 (15), 3401–3414.
Wang, B., Gupta, R., Bei, L., Wan, Q., Sun, L., 2023a. A review on gasification of municipal solid waste (MSW): syngas production, tar formation, mineral transformation and industrial challenges. Int. J. Hydrogen Energy.
Wang, D., Ali, M.A., Alizadeh, A. ad, Singh, P.K., Almojil, S.F., Alali, A.F., Almoalimi, K. T., Almohana, A.I., 2023b. Thermoeconomic appraisal of a novel power and hydrogen cogeneration plant with integration of biomass and geothermal energies. Int. J. Hydrogen Energy.
Wang, J., Yang, Y., 2016. Energy, exergy and environmental analysis of a hybrid combined cooling heating and power system utilizing biomass and solar energy. Energy Convers. Manag. 124, 566–577.
Wang, J., Zhang, S., Xu, D., Zhang, H., 2022. Catalytic activity evaluation and deactivation progress of red mud/carbonaceous catalyst for efficient biomass gasification tar cracking. Fuel 323, 124278.
Wang, S., Lin, H., Abed, A.M., Sharma, A., Fooladi, H., 2022. Exergoeconomic assessment of a biomass-based hydrogen, electricity and freshwater production cycle combined with an electrolyzer, steam turbine and a thermal desalination process. Int. J. Hydrogen Energy 47 (79), 33699–33718.
Wang, Y., Cao, Q., Liu, L., Wu, Y., Liu, H., Gu, Z., Zhu, C., 2022. A review of low and zero carbon fuel technologies: achieving ship carbon reduction targets. Sustain. Energy Technol. Assessments 54, 102762.
Wei, H., Su, C., Dai, J., Albdeiri, M.S., Alsenani, T.R., Elattar, S., Abed, A.M., Hua, Y., 2023. Towards a sustainable, and economic production future: proposing a new process for methanol production based on renewable hydrogen. J. Clean. Prod. 389, 135976.
Wei, X., Manovic, V., Hanak, D.P., 2020. Techno-economic assessment of coal-or biomass-fired oxy-combustion power plants with supercritical carbon dioxide cycle. Energy Convers. Manag. 221, 113143.
Xiao, Y., Wu, S., Xia, H., Zhang, J., Ding, L., Bao, X., Tang, Y., Qi, Y., 2023. Simulation of and multi-aspect study of a novel trigeneration process for crude helium, liquefied natural gas, and methanol production; operation improvement and emission reduction. Fuel 347, 128402.
Xie, N., Xiao, Z., Du, W., Deng, C., Liu, Z., Yang, S., 2023. Thermodynamic and exergoeconomic analysis of a proton exchange membrane fuel cell/absorption chiller CCHP system based on biomass gasification. Energy 262, 125595.
Yang, G., Fan, Z., Li, X., 2019. Determination of confined fluid phase behavior using extended Peng-Robinson equation of state. Chem. Eng. J. 378, 122032.
Yu, D., Duan, C., Gu, B., 2023a. Design and evaluation of a novel plan for thermochemical cycles and PEM fuel cells to produce hydrogen and power: application of environmental perspective. Chemosphere 334, 138935.
Yu, D., Guo, J., Meng, J., Sun, T., 2023b. Biofuel production by hydro-thermal liquefaction of municipal solid waste: process characterization and optimization. Chemosphere 328, 138606.
Zang, G., Zhang, J., Jia, J., Lora, E.S., Ratner, A., 2020. Life cycle assessment of power-generation systems based on biomass integrated gasification combined cycles. Renew. Energy 149, 336–346.
Zhu, L., He, Y., Li, L., Lv, L., He, J., 2018. Thermodynamic assessment of SNG and power polygeneration with the goal of zero CO2 emission. Energy 149, 34–46.